TESI DI DOTTORATO

UNIVERSITÀ DEGLI STUDI DI NAPOLI “FEDERICO II”

DIPARTIMENTO DI INGEGNERIA BIOMEDICA, ELETTRONICA
E DELLE TELECOMUNICAZIONI

DOTTORATO DI RICERCA IN
INGEGNERIA ELETTRONICA E DELLE TELECOMUNICAZIONI

DENOISING OF SAR IMAGES

MARIANA PODERICO

Il Coordinatore del Corso di Dottorato	Tutori
Ch.mo Prof. Niccolò RINALDI	Ch.mo Prof. Luisa VERDOLIVA
	Ch.mo Prof. Giovanni POGGI

A. A. 2011–2012

Contents

List of Figures

Introduction

Remote Sensing images are one of the most effective way to monitor the Earth surface in order to have a read and constant update regarding the evolution of the natural phenomena. This is one of the main reason behind the increasing interest for remote sensing products in many fields of application, from homeland security to environmental protection or land resource management, just to quote some.

Particulary relevant among remote sensors for data acquisition, are the Syntetic Aperture Radars (SAR). SAR is an active coherent sensor which stimulates the scene of interest through electromagnetic waves reproducing it by recording the backscattered signal; such a signal is thus managed by the SAR system up to the imaging processing, in order to obtain the image. The interesting feature of the SAR compared with other sensors such as the optical one, is its microwave nature. This property offers the advantage of working with all weather and illumination conditions. Moreover varying the working frequency and so the penetration depth of the electromagnetic radiation, the information recorded can be about the Earth surface, subsoil, hidden objects.

Although SAR images are a powerful tool, their interpretation is not so easy: in fact, SAR images are affected by a strong noise called speckle, which degrades the performance of many image processing tasks, such as image segmentation, target detection and classification, or recognition of regions of interest by expert human photointerpreter.

These considerations motivate the increasingly interest for reliable despeckling techniques which reduce the speckle and at the same time preserve the structures in the images. However, although the image despeckling has been an active field of research for almost thirty years, and a large number of algorithms have been proposed, performance assessment is still an open issue for real SAR image because of the lack of a reference which does not allow to introduce objective measurement criteria.

The one described is the context where this Ph.D thesis is placed, facing the issue related to the despeckle and performance assessment. Main elements of innovation are the introduction of SAR-BM3D, a denoising algorithm optimized for SAR data, and the introduction of a benchmark which allows measuring and comparing algorithm performance on real SAR images.

One of the main features of the real surfaces is related to their rugosity: provided that such rugosity is in the order of magnitude of the wave lengths used for the investigation, it may happen that surfaces which may seem macroscopically homogeneous are represented with different gray intensity, because of their microscopic structure. In fact the returning echo is the sum of several elementary contributions, each one with its relative delay. Interference caused by different scattering waves can be both constructive and disruptive and may vary between different resolution elements: this is the reason why adjacent cells, even if belonging to images from homogeneous surfaces, may result in very different contributions. This explains why SAR images are characterized by the speckle caused by dark spots, corresponding to disruptive interferences, and clear spots, due to constructive ones. Speckle is thus defined as a signal-dependent random noise, which is stronger in clearer areas.

Many algorithms have been proposed in the SAR denoising literature to reduce the speckle. The interchanging of two main approaches *i.e.* the homomorphic one, which turns into additive the multiplicative noise through a logarithmic transform and the non-homomorphic one, which takes into account multiplicative nature of noise to develop the algorithm, outlines the SAR denoising context. This is characterized by the early spatial domain techniques which have led way to the wavelet based algorithms in the last 80s. A complete change of perspective is the introduction of the non-local filtering which bases its power on the exploiting of the contextual information, like Non-Local Means (NLM) and Block-Matching 3D (BM3D) algorithms developed in AWGN hypothesis; the latter, considered the state-of-the-art, has obtained relevant results with the readily extension of NLM to SAR despeckling. In this scenario we propose SAR-BM3D algorithm which is the extension of the BM3D concepts in the context of despeckling, optimizing the elaboration for SAR data and following a non-homomorphic approach. A very detailed experimental analysis on artificially speckle corrupted images will prove that SAR-BM3D is performing better respect traditional approaches, both in terms of PSNR and visual inspection.

Well known are the difficulties in evaluating denoising techniques performance on real SAR image. Only partial parameters, like the Equivalent Number of Look (ENL), which measures the reduction of speckle in flat areas, are used by the researcher with no information about feature preservation. Nowadays, neither objective and exhaustive parameters to evaluate performance are available, nor a simple set of benchmark images which allow for a clear evaluation of algorithms has been found. In fact stating the reliability of the comparison on the speckle corrupted natural images, we want to outgo dealing with problem of difference between the optical reference such as natural image and SAR reference. As consequence we have investigated the possibility to create images more similar to the real SAR images. So with the cooperation of the remote sensing group of the University of Naples Federico II, which has developed a SAR simulator, we have accurately selected and used some test cases created by the SAR simulator. Main advantage of the so called SARAS images is the availability of both the artificially corrupted and the original one, which can be taken as reference in order to evaluate the performance of different algorithms. We will show in details the procedure which leads to a definition of an objective criterion to compare results provided by different algorithms when performing on real SAR images. For this purpose, appropriate measurements for characterization of each test case will be provided.

The thesis is organized as follows:

Chapter 1 introduces SAR images and the related problem of speckle. In particular, it describes the statistical properties of these images, focusing on the multiplicative random nature of the speckle noise and on the basic assumptions done on SAR data elaborations, known in literature.

Chapter 2 is dedicated to outline the context of SAR denoising, describing the most effective way to deal with the multiplicative speckle model. In particular we distinguish two main approaches: the homomorphic and non-homomorphic one, which have been developed over the years in spatial domain, wavelet domain and non-local techniques. Furthermore we introduce the basic concepts that have inspired the development of the proposed algorithm SAR-BM3D.

Chapter 3 presents the innovative SAR-BM3D in details. Starting from key elements of wavelet based and non-local filtering, SAR-BM3D optimizes the elaboration for SAR data, following a non-homomorphic approach. A deep experimental analysis on artificially speckle corrupted images has been performed, to compare SAR-BM3D with other traditional approaches, both in terms of PSNR and visual inspection.

Chapter 4 addresses the difficulties in evaluating denoising techniques performance on real SAR images. It shows in details the procedure which leads to a definition of an objective criterion to compare results provided by different algorithms, using images obtained by a SAR simulator. Main advantage of these images is the availability of both the speckled image and the noise-free one, which can be taken as reference in order to evaluate the performance.

Chapter 1

SAR images and speckle

Because of the coherent nature of Synthetic Aperture Radar (SAR), the acquired images are characterized by a strong noise called speckle, which has a multiplicative random nature. Speckle, which appears with a typical grain effect, is due by the interference phenomena of the coherent waves echoes reflected by the elementary scatterers within the SAR resolution cell. In this chapter we focus our attention on the fundamental properties of SAR images and the problems related to the statistical model of the speckle noise.

1.1 Statistical properties of SAR images

The objective of SAR processing is the reconstruction of the Earth surface by the target's scattered contributions, received by the SAR antenna and recorded in the memory. The main feature of such a system is the resolution cell whose size depends on the azimuth (Δa) and range (Δr) resolution and which describes the smallest object the system is able to recognize [1].

Usually, given a resolution elementary cell, the assumption is to deal with punctiform objects. In our case, being the size of such elementary cells up to several meters, this assumption is not correct: the cell itself may in fact contain several scattering points, so signal reflection may occur following different paths. One of the main features of the real surfaces is related to their rugosity: provided that such rugosity is in the order of magnitude of the wave length used for the investigation, it may happen that surfaces which may seem macroscopically homogeneous are represented with different gray intensity, because of their microscopic structure. For this reason the returning echo is the sum of several elementary contributions, each one with its relative delay, which can

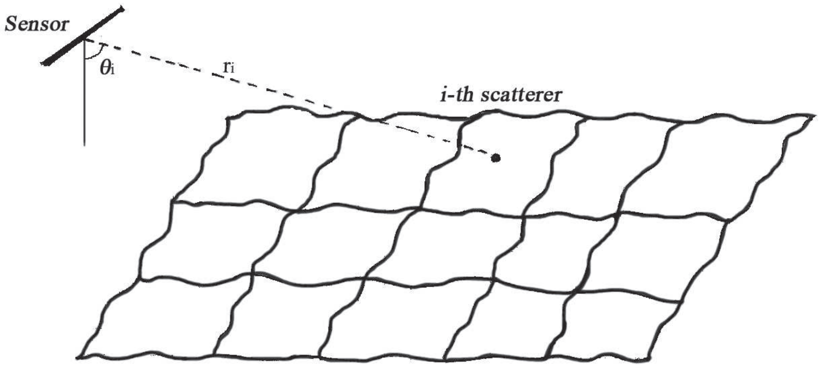

Figure 1.1: Distributed target.

be in the range of few up to several wave lengths. Interference caused by different scattering waves can be both constructive and disruptive and may vary between different resolution elements: this is the reason why adjacent cells, even if belonging to images from homogeneous surfaces, may result in very different contributions. This explains why SAR images are characterized by dark spots, corresponding to disruptive interferences, and clear spots, due to constructive ones. Generally, a statistical approach is followed to study the speckle because it is difficult to know the scene statistics. Based on the considerations above, let try to arrange a statistical representation of the scattered field in order to have a model to use as reference.

Assume we have a coherent sensor, which reveals the absolute and phase value of the scattered field. Suppose we have distributed targets, then we can think that in each resolution cell there are a number N_s of discrete scatterers (Fig. 1.1). The electromagnetic echo of the i-th scatterer is

$$e_i = Re\left[E_i e^{jwt}\right] \tag{1.1}$$

where the phasor E_i has the following expression:

$$E_i = K_i E_i e^{j\theta_i} e^{-j2kr_i} \tag{1.2}$$

where

- r_i is the distance between the radar and the scatterer;
- K_i is an attenuation factor ($K_i \propto 1/r_i$);

- $E_i e^{j\theta_i}$ is the incident phasor field[1];
- e^{-j2kr_i} is the phase displacement of the incident field to cover a round trip;

Now we explain some hypotheses to make the model of simple application:

- **hp 1:** each element is an *independent* scatterer, *i.e.* the echoes are independent from each other. So the total backscatter of the incident wave is the sum of all the contributes:

  $$E = \sum_{i=1}^{N_s} K_i E_i e^{j\varphi_i} \tag{1.3}$$

  where $\varphi_i = \theta_i - 2kr_i$

  Assuming independent contributions for each scatterer is an hypothesis verified only if different scatterers do not influence each other, which means the rugosity of the surface is not so high and there are no *corner reflectors*[2] to avoid multiple reflections;

- **hp 2:** the sensor is in the far filed zone with reference to the illuminated scene. So the distance between sensor and scatterers is

  $$r_i \gg (\Delta_a, \Delta_r) \tag{1.4}$$

  where Δ_a e Δ_r are the sizes of the resolution cell. So all the attenuation coefficients K_i are equal[3]. Then we obtain:

  $$K_i = K = 1 \ \forall i \Rightarrow E = \sum_{i=1}^{N_s} E_i e^{j\varphi_i} \triangleq V e^{j\varphi} \tag{1.5}$$

- **hp 3:** the scatterers number N_s is very large:

  $$N_s \gg 10 \Rightarrow (\Delta_a, \Delta_r) \gg \lambda \tag{1.6}$$

---

[1] Here we consider the scalar value of the incident field and not the vector.

[2] *Corner reflector* is a structure with three incident orthogonal planes, such as building and house, so all the incident waves are reflected to the source without overlapping.

[3] We suppose to make a zero order approximation for the multiplicative terms depending on r; it is not possible to make an analogous approximation for the phase.

- **hp 4:** E_i and φ_i are independent from each other; in the case of a random scene, this hypothesis is licit because E_i depends on the terrain nature (*i.e.* on the terrain electromagnetic features described by the complex dielectric constant ε^4 and the magnetic permeability μ, respectively), while φ_i depends mostly by r_i. So the absolute and phase values of a single echo are all independent from each other. Ideally, if we have a flat surface phases of each element could be deterministically correlated. When, on the contrary the surface is not flat there is a random path difference which increases with the rugosity.

- **hp 5:** φ_i e φ_j are independent random variables $\forall i \neq j$ and are uniformly distributed in $(0, 2\pi)$. This is a licit assumption due the random distributed scene and the rugosity proportional to some wavelengths.

- **hp 6:** all the scatterers are *identically distributed*, so none is dominant; *i.e.* there are no *corner reflectors* in each resolution cell.

Due to these statements, for large numbers of *i.i.d.* (independent and identically distributed) scatterers we can apply the *Central Limit Theorem*, CLT, [2]. So we have

$$V_x \triangleq Re\left\{Ve^{j\varphi}\right\} = \sum_{i=1}^{N_s} E_i \cos\varphi_i \tag{1.7}$$

$$V_y \triangleq Im\left\{Ve^{j\varphi}\right\} = \sum_{i=1}^{N_s} E_i \sin\varphi_i \tag{1.8}$$

where V_x e V_y are Gaussian random variables $\mathcal{N}(0, \sqrt{\sigma/2})$.

Because of:

$$E[V_x] = \sum_{i=1}^{N_s} E[V_i \cos\varphi_i] = \sum_{i=1}^{N_s} E[V_i]E[\cos\varphi_i] = 0 \tag{1.9}$$

and

$$E[V_xV_y] = \sum_i \sum_j E[V_iV_j]E[\cos\varphi_i \sin\varphi_j] = 0. \tag{1.10}$$

V_x e V_y are independent, being Gaussian and uncorrelated, with joint probability density:

$$p(V_x, V_y) = \frac{1}{\pi\sigma} e^{-\frac{V_x^2+V_y^2}{\sigma}} \tag{1.11}$$

---

[4] The real part of ε defines the reflected waves features, the imaginary part the absorbed energy in the media.

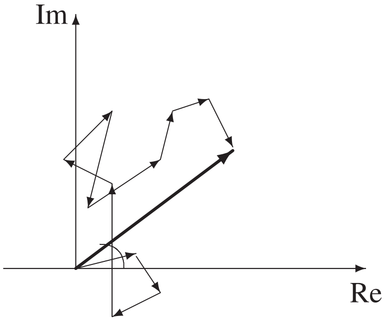

Figure 1.2: Random walk in the complex plane

With this assumption, the backscatter field looks like a random walk in the complex plane (Fig. 1.2).

In polar coordinates, we have:

$$p(V_x, V_y)dV_x dV_y = p(V_x, V_y)V dV d\varphi = p(V, \varphi)dV d\varphi \tag{1.12}$$

where V is the Jacobiano. By comparison between the equations 1.11 and 1.12 and solving with reference to $p(V, \varphi)$ we obtain:

$$p(V, \varphi) = \frac{V}{\pi\sigma} e^{-\frac{V^2}{\sigma}} \tag{1.13}$$

where

$$V = \sqrt{V_x^2 + V_y^2} \triangleq A \in [0, \infty) \tag{1.14}$$

and

$$\varphi \in (0, 2\pi) \tag{1.15}$$

They have the following distributions, respectively:

$$p(A) = \int_0^{2\pi} p(A, \varphi)d\varphi = \frac{2A}{\sigma} e^{-\frac{A^2}{\sigma}} \tag{1.16}$$

$$p(\varphi) = \int_0^{\infty} p(A, \varphi)d\varphi = \frac{1}{2\pi}. \tag{1.17}$$

So the absolute value (called A *amplitude*) of the electromagnetic backscatter is *Rayleigh* distributed in $[0, \infty)$, while the phase is *Uniformly* distributed in $[0, 2\pi]$.

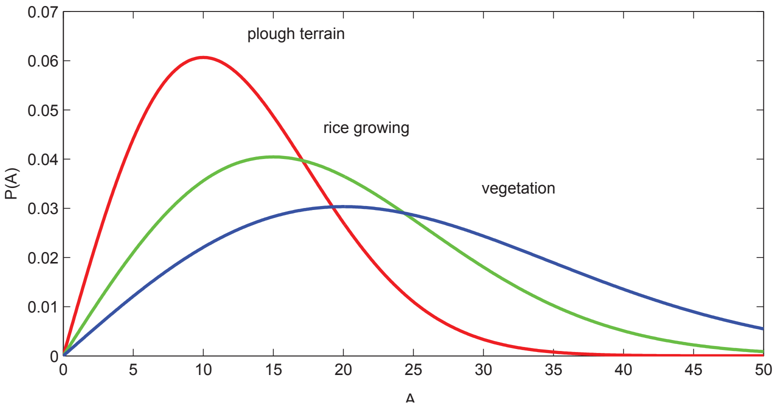

Figure 1.3: *Rayleigh* distributions of different areas.

If we consider a linear detector which reveals the amplitude A of the field, the statistical characterization is the following:

$$E[A] \triangleq \int_0^\infty A p(A) dA = \frac{\sqrt{\pi\sigma}}{2} \tag{1.18}$$

$$E[A^2] \triangleq \int_0^\infty A^2 p(A) dA = \sigma \tag{1.19}$$

$$\sigma_A^2 = E\left\{(A - E[A])^2\right\} = E[A^2] - E[A]^2 = \frac{4-\pi}{4}\sigma \tag{1.20}$$

Note that mean and variance of the amplitude are correlated because the *Rayleigh* distribution has only one parameter.

Since the amplitude of the backscatter field of a resolution cell is a random variable, we can think a macroscopically homogeneous area as a random variables collection, *i.e.* as a *random process*. So a macroscopically homogeneous area presents a *Rayleigh* distributed echo and so it is not univocally described by only one gray level, but by all the gray levels of the considered scale, depending on the distribution standard deviation, which is an estimation of the signal fluctuations around its mean value (Fig. 1.3). If we consider a quadratic detector, the measured quantity is the field power, called intensity I, $I = A^2$. It follows that:

$$p(A)dA = p(A)2AdA = p(I)dI \tag{1.21}$$

so the *pdf* is:

$$p(I) = \frac{1}{\sigma} e^{-\frac{I}{\sigma}} \tag{1.22}$$

The field intensity has an *Exponential* distribution. Its statistical characterization is the following:

$$E[I] = E[A^2] = \sigma \tag{1.23}$$

$$E[I^2] = 2\sigma^2 \tag{1.24}$$

$$\sigma_I^2 = \left\{(I - E[I])^2\right\} = E[I^2] - \{E[I]\}^2 = \sigma^2 \tag{1.25}$$

The standard deviation σ_I is the estimation of the signal fluctuations around its mean value. Therefore we can assume that either for the linear or quadratic detector, the fluctuations around the mean value are caused by the noise. If we consider that:

- the mean value is the signal (an estimation of the signal);
- all the fluctuations, expressed by the standard deviation, are considered noise;

it has sense to define the *Intrinsic Signal to Noise Ratio*, ISNR, which is for linear detector:

$$\text{ISNR} \triangleq \frac{\{E[A]\}^2}{\sigma_A^2} = \frac{\pi}{4-\pi} = 5.6\,\text{dB} \tag{1.26}$$

and for quadratic detector:

$$\text{ISNR} \triangleq \frac{\{E[I]\}^2}{\sigma_I^2} = 1 = 0\,\text{dB} \tag{1.27}$$

Note that in the hypothesis of the CLT, the number of the scatterers N_s is very large and the scatterers are identical distributed, so the fluctuations of the signal are caused only by speckle. In this case we refer to speckle such as the *fully developed* speckle. However in other important situations this model fails. Indeed the number of contributions in a resolution cell is always finite (this is the case of the texture such as woods or fields, as well as discrete objects, such as individual trees, edges, roads and buildings) and the statistics of speckle generated by a finite number of field contributions are different from those for the usual model [3].

In some circumstances N_s may become small so that the speckle is no more considered *fully developed* and cannot be modeled any more with previous distributions [1]. In this section, we will not deal with this case because of the vastity of the argument. But it is important to know that the *fully developed* speckle is not the only case that we can observe in a SAR image.

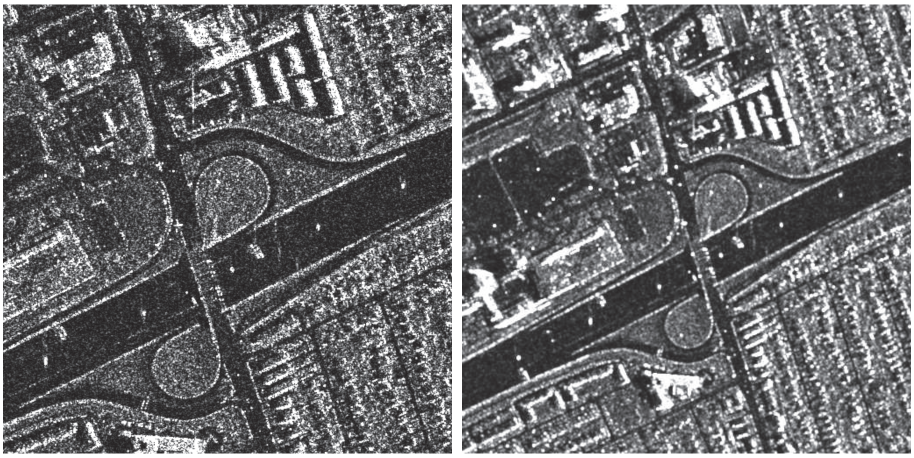

(a)Toronto, L=1 (b)Toronto, L=6

Figure 1.4: Toronto (©Infoterra GmbH) and its intensity multilook version.

1.2 Multilook data

As we said in the previous section, both in the linear and quadratic detector, the parameter of interest is σ, which carries information about the target. From the equation (1.23) we can see that it is the average intensity. It can be proved, by simply computations, that given the field components V_x and V_y, we can compute the *Maximum Likelihood Estimate*, MLE, at each pixel of σ, which is the average intensity.

To reduce the fluctuations of the signal and so to improve the estimates of σ there is a technique called *multiple look processing* (multilook). The multilook is the statistics average of L independent measurements of the same resolution cell (of the same random process). This will preserve the mean value and at the same time reduce the variance of a factor L. Due to these observations and recalling that σ is the average intensity, this suggests that the multilook has to be computed in intensity, obtaining an incoherent average. Also in this case it is easy to show that the intensity multilook is the MLE estimator of σ. An example of intensity multilook is provided in (Fig. 1.4) for the TerraSAR-X image of Toronto. It's interesting to note that the amplitude average of the data gives a worse estimate compared to the intensity one. It is clear observing the equation (1.18). Moreover the (1.9) formula shows that averaging complex data has no sense because each component has zero mean.

It is possible to generate multilook in several other ways: frequency, temporal or spatial domain multilook. In all the cases, even if for different reasons, the disadvantage is that a lack of resolution occurs. It is interesting to consider expression of the L-look data *pdf* in the intensity and amplitude case. The L-look average intensity follows a gamma distribution with order parameter L [1]

$$P_I(I) = \frac{1}{\Gamma(L)}\left(\frac{L}{\sigma}\right)^L I^{L-1}e^{-LI/\sigma} \quad I \geq 0 \tag{1.28}$$

with moments

$$< I^m >= \frac{\Gamma(m+L)}{\Gamma(L)}\left(\frac{\sigma}{L}\right)^m . \tag{1.29}$$

For what concerns the amplitude data $A = \sqrt{I}$, the expression of the multilook *pdf* is due to the multi-convolution of the Rayleigh probability density which has not a closed-form. So to circumvent this problem it is often used the square root of the intensity multilook *pdf*, which is an approximation of the real *pdf*. So in this case we obtain the square root gamma distribution

$$P_A(A) = \frac{2}{\Gamma(L)}\left(\frac{L}{\sigma}\right)^L A^{2L-1}e^{-LA^2/\sigma} \quad A \geq 0 \tag{1.30}$$

which is derived from (1.28) using the change of variable

$$P_A(A) = 2AP_I(A^2) \tag{1.31}$$

This distribution has the following moments

$$< A^m >= \frac{\Gamma(L+m/2)}{\Gamma(L)}\left(\frac{\sigma}{L}\right)^{m/2} \tag{1.32}$$

1.3 Multiplicative speckle model

In section 1.1 we derive a discrete scatterer model which describes how the radar waves interact with a distributed target. This model implies that at each pixel in the SAR data all the information is carried by the mean of the incoherent power σ, (1.23). If the observed intensity at each pixel shows the conditional probability

$$P_I(I/\sigma) = \frac{1}{\sigma}e^{-I/\sigma} \quad I \geq 0 \tag{1.33}$$

making the following change of variables

$$I = \sigma n \tag{1.34}$$

we obtain the pdf of n

$$P_n(n) = e^{-n} \quad n \geq 0 \tag{1.35}$$

So, the observed intensity can be considered as a deterministic value σ which modulates a unit mean exponentially distributed speckle n. Here we have used n to indicate the speckle, being its properties similar to noise ones. Obviously, a similar decomposition (1.34) states for L-look data, where n is a unit mean gamma distributed variable with order parameter L. This formulation of the SAR image, as a deterministic value of interest σ which multiplies a random stationary speckle process, justifies the description of speckle as multiplicative noise. This model known as *fully developed* speckle model is verified only in homogeneous areas. In fact, in this case macroscopic features are truly regards as a deterministic value σ, while the microscopic behavior, caused by the natural roughness, which determines the presence of speckle, is accounted for through a statistical model.

For L-look intensity data, I can be expressed in the same way, where the speckle is distributed as

$$P(n) = \frac{L^L n^{L-1}}{\Gamma(L)} \exp(-Ln) \tag{1.36}$$

As we said above, normally, this model known as *fully developed* is exploited when the fluctuations of the speckle and signal are on very different spatial scales, so they do not interact and can be separated. This is the case of homogenous areas. When it is not the case, and so signal fluctuations cannot be separated by speckle ones, because they are on the same spatial scales, this model fails.

A significant step further in the modeling of radar image properties is to englobe the behavior of the underlying scene fluctuations in (1.34). Given a distribution of the original signal $P(\sigma)$, the product model describes the observed intensity *pdf* as

$$P(I) = \int_0^{+\infty} P(I|\sigma)P(\sigma)d\sigma = \frac{L^L I^{L-1}}{\Gamma(L)} \int_0^{+\infty} \frac{d\sigma}{\sigma^L} \exp\left(-\frac{LI}{\sigma}\right) P(\sigma) \tag{1.37}$$

So the product model separates two distinct processes: the speckle, caused by the random distribution of the scatterers, and the original signal, which depends on the physical properties of those scatterers [1]. This model is of great interest because it takes into account the features of natural clutters as forests, woodlands and so on, very common in SAR images.

1.4 SAR system and imaging effect

The analysis of the previous sections was in terms of the given data and ignored how the imaging process affects the information carried by the data. In fact, although we have chosen to focus only on the final products of the system, the complex images, it must be remembered that SAR in an extremely complex system, involving a number of processing steps that certainly affect the quality of the final image. The raw data collected by the sensor must be quantized and possibly compressed [4, 5], and sent to an Earth station through a physical band-limited channel, where a complex focusing process finally takes place.

Essentially there are three imaging effects which must be taken into account when trying to recover the backscattering coefficient σ

1. a scaling of σ due to propagation, antenna pattern and processing effects;
2. a bias in σ due to system noise;
3. spatial correlation induced by the processing.

In this section for sake of simplicity we want to consider only the effect listed in the third point e.g. the spatial correlation induced by the processing, neglecting all others factors.

The effects of the correlation are taken into account trough the point spread function (PSD) of the SAR system. Indeed, the imaging process in a SAR system, assuming the linearity and the translation invariance of the system (LTI), can be described with the complex function

$$h(k) = p(k) + jq(k) \tag{1.38}$$

If the complex reflectivity of the Earth's scene is

$$\gamma(k) = x(k) + jy(k), \tag{1.39}$$

the complex image is

$$i(k) = a(k) + jb(k) = h(k) * \gamma(k), \tag{1.40}$$

where the star denotes the convolution operation and the intensity image is $I(k) = |i(k)|^2$.

For sake of simplicity, we assume that the signal $\gamma(k)$ describes a uniformly distributed target. In this case its components x and y are Gaussian random variables, such as $\mathcal{N}(0, \sqrt{\sigma/2})$, and its *autocorrelation function* (acf) is

$$R_\gamma(\tau) = \sigma\delta(\tau). \tag{1.41}$$

As a consequence the components of the complex image, $a(k)$ and $b(k)$ respectively, will be Gaussian, such as $\mathcal{N}(0, \sqrt{\sigma E/2})$, where $E = \int |h(k)|^2 dk$ is the energy of the SAR system. Here, to simplify the computation we assume $E = 1$.

Recalling the autocorrelation input-output relations of a LTI system ($R_i(\cdot) = R_\gamma(\cdot) * R_h(\cdot)$), the coherent acf is

$$R_i(\tau) = \sigma\delta(\tau) * R_h(\tau) = \sigma R_h(\tau) \tag{1.42}$$

where R_h is the acf of the SAR system and $E = R_h(0) = 1$.

So the acfs of the components a and b of the complex image are related to R_h in the following way:

$$R_a(\tau) = R_b(\tau) = \frac{\sigma}{2} Re\{R_h(\tau)\} = \frac{\sigma}{2}(R_p(\tau) + R_q(\tau)) \tag{1.43}$$

and

$$R_{ab}(\tau) = -R_{ba}(\tau) = -\frac{\sigma}{2} Im\{R_h(\tau)\} = \frac{\sigma}{2}(R_{pq}(\tau) - R_{qp}(\tau)) \tag{1.44}$$

Notice that $R_{qp}(\tau) = R_{pq}(-\tau)$, so $R_{ab}(0) = 0$, *i.e.* a e b are uncorrelated in the zero point. Since they are normal, they are independent, so the intensity image $I(k) = |i(k)|^2$ will be distributed exponentially with mean $\sigma_I = \sigma$. The intensity acf is then due to the Siegert relation [6]:

$$R_I(\tau) = \sigma_I^2(1 + |R_h(\tau)|^2) \tag{1.45}$$

Getting from (1.42) $R_h(\tau) = R_i(\tau)/\sigma$ we obtain the relation which connects the intensity and complex image acf

$$R_I(\tau) = \sigma^2(1 + \frac{|R_i(\tau)|^2}{\sigma^2}) \tag{1.46}$$

Note that if the distributed target is not uniform, coherent acf function remains unchanged while I acf becomes more complex. So, in case of uniform distributed target the way the SAR system autocorrelation function does affect data can be easily foreseen, while in case of texture this becomes more complex to do. In case unknown SAR system acf, it can be estimated based on the available samples of the speckle affected images, provided to have them in intensity format. Such estimation and correction procedures require average and subsampling techniques. Being the SAR system sampling frequency required, such techniques are not simple to be implemented; besides, a lack of information is caused. This is the reason why nowadays all the denoising algorithms do not take into account this peculiarity of SAR images. Usually both the correlation between speckle and signal and different speckle samples is considered to be negligible, so as a result the elaboration is suboptimal [6].

Chapter 2

Denoising SAR: state of the art

As we show in the previous chapter, since SAR sensors have a coherent nature the obtained images are affected by a strong multiplicative noise, called speckle. As a consequence, detecting objects and regions of interest in SAR images may be a very difficult task even for an expert human interpreter, and prohibitive for automatic algorithms of segmentation or classification. For this reason some sort of denoising is needed [1]. A first stage to reduce the speckle is an incoherent average, the multilook, which reduces the intensity noise variance with the drawback of a resolution loss. So a more sophisticated denoising approach is necessary to reduce the noise and at the same time preserve the image features. In this chapter we analyze the SAR denoising scenario, focusing on the more famous and efficient approaches, which represent the state-of-the-art. In this way, we outline the context which has encouraged the main idea of the proposed algorithm SAR-BM3D, explained more in detail in the next chapter.

2.1 Homomorphic and non-homomorphic approach

When the speckled images have started to spread in the scientific community many researchers dealt with the problem of filtering images affected by a multiplicative random noise. The early speckle reduction techniques were developed following two main approaches: the homomorphic and non-homomorphic approach.

Homomorphic approach

The homomorphic approach was born to take advantage of most available filtering algorithm developed for additive white Gaussian noise (AWGN). It consists in applying a logarithmic transform of the data to convert the multiplicative noise in an additive one.

Since the non linearity of the logarithmic transform the statistics of SAR images are totally changed, so it is necessary a detailed analysis of the distribution and statistics of the log-transformed speckle. As consequence over the years many authors have proposed studies to describes the characteristics of the log-transform random variables. Arsenault *et al.*, [7], showed that the logarithm of speckle noise approaches a normal distribution, increasing the number of look L.

In a more recent work Xie *et al.* [8] derives the probability density functions and the statistics to characterize the log-transformed speckle, discussing at the same time the problems introduced by the logarithmic transform on analysis of SAR images. In fact the log-transformed speckle is non-Gaussian, especially in the important single-look case and has non-zero mean, whereas a significant set of techniques assume a zero mean AWGN noise. In general, mean bias problem should not be ignored especially for SAR images with high noise levels, for the purpose of radiometric preservation. So it is necessary to correct the biased mean within the processing stages. More important, the logarithm changes radically the data dynamics, leading to unavoidable radiometric distortions during the denoising process.

Non-homomorphic approach

The non-homomorphic approach consists in exploiting the multiplicative noise model to develop the denoising algorithm. To one side this brings the advantage that all the issues related to the homomorphic approach are avoided, on the other side there is a modeling problem when dealing with the multiplicative model.

Some of the early techniques, which approache the multiplicative model were not as well developed as the techniques for additive noise. Over the years lot of techniques have been proposed, which exploite the non homomorphic method such as [9] [10], [11], [12] [13], [14], enumerating only the spatial domain approaches. All such techniques simplify the multiplicative noise model in various ways, *e.g.* through its linear approximation [9] or recasting it as a signal-dependent additive noise model in the following way

$$z(s) = x(s)u(s) = x(s) + [u(s) - 1]x(s) = x(s) + u'(s)x(s) = x(s) + v(s), \tag{2.1}$$

where $v(s)$ is the zero-mean, signal-dependent additive noise uncorrelated with x.

In the following sections we describe the evolution of the SAR denoising techniques, through the interchanging of homomorphic and non-homomorphic approaches in the context of spatial domain, wavelet domain and non-local techniques, respectively.

2.2 Spatial domain techniques

From a signal processing perspective, despeckling filters approach the problem of denoising as a statistical estimation issue, performing an estimate of the radar reflectivity (the signal of interest), through a direct manipulation of the speckled image (the noisy observed signal) [15].

In the context of estimation theory, a measurement of a stochastic process, observed in a finite interval, leads to meaningful parameters estimations only if the process is ergodic and stationary. We recall that ergodicity is required to approximate the ensemble average with the sample average, and the stationarity ensures that the estimations computed on a finite interval approximates the estimations on the whole process. Thus an interesting way to catalogue and describe the speckle filtering is as a function of the stationarity and non stationarity nature of the scene, speckle, and observed signals. Usually most of the speckle filters assume that speckle noise is a multiplicative unit mean wide sense stationary process. This assumption simplifies the processing since speckle statistics, constant on the whole scene, are estimated only once.

However we can distinguish two categories of speckle filters with reference to the assumptions about the stationarity-non stationarity nature of the speckle random process, as follows:

1. Stationary Multiplicative Speckle Model Filters (SMSM filters): assume the speckle stationary over the whole image. We recall the Lee [9], the Frost et al. [11], and the Kuan et al. [12] filters. These filters are based on the multiplicative speckle model, discussed in details in the previous chapter.

2. Non-stationary Multiplicative Speckle Model Filters (NSMSM filters): assume that speckle is not locally stationary within the filter window.

These filters, such as the MAP Gaussian filter [16], are based on the product model, thus the intensity speckle mean is non stationary.

2.2.1 SMSM filters

The most well known SMSM filters which are based on the stationarity assumption of the multiplicative speckle model are the Lee and Kuan MMSE filters, as well as the Frost filter. They carry out the despeckling in the original domain (non log-transformed), *i.e.* in a non-homomorphic way.

All such techniques operate in the spatial domain with linear filters developed under a MMSE (minimum mean-square error). By the theory, assuming Gaussian signals, the MMSE solution becomes a linear function of the covariance matrix of the signal and noise. In this case it is called linear MMSE (LMMSE) filtering [17]. Generally the LMMSE approach is very interesting because does not require a high computational cost, depending only on the first two moments of the *pdf*.

Due to the spatial variations of the scene signal, the measured radar signal $z(s)$ is not generally stationary, so Lee [9], Kuan [12] and Frost [11], although in different way, were the first to apply the LMMSE filtering in a local way, introducing the idea of adaptive filtering. In fact, supposing that signals are *stationary in increments*, *i.e.* locally stationary, the first two moments required to apply the LMMSE approach are accurately estimated within a moving window. In particular in [9] and [12], is exploited the assumption of uncorrelated signal variations around its space-varying mean. In [11] is applied an LMMSE approach by locally modeling the covariance matrix of the signal.

These early papers make already clear that some kind of local adaptivity is necessary to account for the non stationarity of the image: the intense smoothing required to reduce speckle in homogeneous areas cannot be applied in edge and textured regions lest important structural information gets lost. Contextual information is hence taken into account, in various ways [10], [13], [14] to adapt the filters to local image behavior.

To conclude the description of SMSM filters it is worth to spend some more words on the local LMMSE approach developed for additive signal-dependent noise [12], because it is recalled in many other techniques.

Local Linear MMSE filtering for additive signal-dependent noise

Here we explain in more details the local minimum mean square error (LLMMSE) filter for additive signal-dependent noise model such as in (2.1). It is worth noting that, due to the independence of x and u, and the fact that u' has zero mean, the additive noise v, whose variance depends on x, is zero-mean and appears to be uncorrelated with x. In the previous hypothesis if **x**, **z** and **v** denote the noiseless reflectance, the observed noisy signal, and the additive signal-dependent noise, expressed such as 1-D vectors of size N, the MMSE estimate of **x** is its conditional expectation to the observed signal

$$\hat{\mathbf{x}}_{MMSE} = E[\mathbf{x}|\mathbf{z}]. \tag{2.2}$$

In general this estimate requires the knowledge of the non stationary probability density functions (*pdfs*) moments of all orders. By making a first order Taylor development of $E[\mathbf{x}|\mathbf{z}]$ around its unconditioned expected value $E[\mathbf{x}]$, we obtain the linear MMSE (LMMSE) estimator defined as

$$\hat{\mathbf{x}}_{LMMSE} = E[\mathbf{x}] + \mathbf{C_{xz}}\mathbf{C_z}^{-1} \cdot [\mathbf{z} - E(\mathbf{z})] \tag{2.3}$$

in which the $N \times N$ matrices $\mathbf{C_z}$ and $\mathbf{C_{xz}}$ are the auto-covariance of **z** and the cross covariance between **x** and **z**, respectively. In this case only signal and noise second order statistics are required.

Assuming **x** spatially uncorrelated, and noise **v** of zero-mean, the global minimization in (2.3) corresponds to a *local* minimization in a neighborhood of each sample. If $E[\mathbf{v}] = \mathbf{0}$, the covariance matrices $\mathbf{C_z}$ and $\mathbf{C_{xz}}$ in (2.3) become diagonal

$$\begin{aligned}\mathbf{C_z} &= \mathbf{C_x} + \mathbf{C_v} \\ &= diag[\sigma_x^2(1) + \sigma_v^2(1), \ldots, \sigma_x^2(N) + \sigma_v^2(N)] \\ \mathbf{C_{xz}} &= \mathbf{C_x} = diag[\sigma_x^2(1), \sigma_x^2(2), \ldots, \sigma_x^2(N)].\end{aligned} \tag{2.4}$$

where $\sigma_x^2(n)$ and $\sigma_v^2(n)$ denote the ensemble variance of **x** and **v** at the *nth* sample position [12]. By replacing (2.4) in (2.3), we obtain

$$\hat{x}_{LLMMSE}(n) = E[x(n)] + \frac{\sigma_x^2(n)}{\sigma_x^2(n) + \sigma_v^2(n)} \cdot \{z(n) - E[z(n)]\}. \tag{2.5}$$

The first order statistics may be locally computed in a neighborhood of the sample n. In fact under the model assumption (2.1), we derive $\sigma_x^2(n)$ and the ensemble statistics are approximated with the local sample statistics.

In other words, the spatial LLMMSE estimator based on local approximations of the non stationary mean and variance of the noise-free image obtained by the noisy image, $\bar{z}(n)$ and $\hat{\sigma}_z^2(n)$, is

$$\hat{x}_{LLMMSE}(n) = \bar{z}(n) + [z(n) - \bar{z}(n)] \cdot \max\left\{0, \left[1 - \frac{\sigma_{u'}^2 \cdot \bar{z}^2(n)}{\hat{\sigma}_z^2(n)}\right]\right\} \frac{1}{1+\sigma_{u'}^2}. \quad (2.6)$$

where $\max\{\cdot\}$ prevents negative value for the estimated signal variance.

Notice that the fundamental assumption for the LLMMSE estimator is that **x** is spatially uncorrelated with $\mathbf{C_x} \triangleq E\{[\mathbf{x} - E(\mathbf{x})][\mathbf{x} - E(\mathbf{x})]^T\}$ a diagonal matrix. Moreover it is required the local ergodicity to estimate the local mean and variance from a neighborhood of samples. These approximations are not verified when an edge occurs, so the filter performance becomes poor.

So assuming a non stationary mean and non stationary variance (NMNV) model and uncorrelated noise, the LLMMSE filter has a very simple structure and it is a point processor.

2.2.2 NSMSM filters

The most well known NSMSM filters that reduce speckle under the non stationarity multiplicative speckle model assumption are proposed in [16], [18], [19]. In contrast to SMSM speckle filters, the NSMSM filters that are based on the product model require the knowledge of the a priori *pdf*. Besides, the simple MMSE estimation is replaced by the more sophisticated and promising Bayesian maximum a posteriori (MAP) approach which, however, brings with it the problem of providing an accurate statistical description of the SAR image.

Several competing models have been proposed in the literature, *e.g.,* the Gamma distribution considered in [18] which leads to the GMAP algorithm. As a matter of fact, this is a challenging and still open problem, and no parametric model, to date, seems able to account for the variety of situations encountered in SAR images [20]. In addition, parameter estimation is by itself a tricky problem, being especially sensitive to the volume of available data (think of local estimation windows), with all inaccuracies translating in artifacts and artificial biases in the reconstructed scene [15]. Indeed if on one side it is needed a large processing window to have an accurate estimate of the *pdf* parameters, on the other hand if the number of independent samples is not large enough, may be introduced a radiometric bias. In particular this bias depends on the number of the window samples but also on the texture autocorrelation included in the window. It is interesting to note that MMSE filter introduces

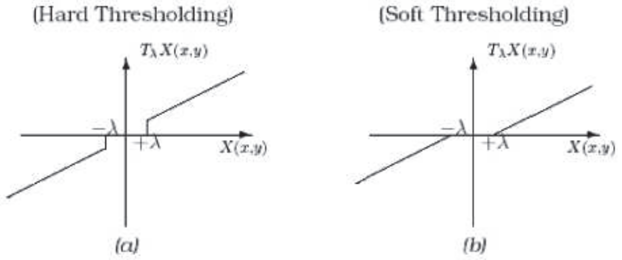

Figure 2.1: Thresholding operators

a very little bias at small window compared to the Gamma MAP filter. Being the MMSE filter based on the stationary assumption of the speckle, it requires fewer independent samples for accurate estimation of the one level statistics. In fact the increase of the window size needed for accurate estimation depends on the number of levels of statistics required.

2.3 Wavelet domain techniques

In the early 90's works such as [21] and [22] ratified the introduction of the wavelets in the signal processing community. The wavelets, recognized as a powerful tool for the analysis of non stationary signals and images, have open the way to a new generation of despeckling techniques based on multiresolution processing. Indeed, Donoho in [23] introduces the concept of denoising in the discrete wavelet transform (DWT) domain, the wavelet shrinkage, exploited as a simple shrinkage of the DWT detail coefficients of the noisy image, based on AWGN hypothesis. Wavelet shrinkage can be applied, with no effort and in a simple way, to reduce the speckle in an homomorphic way.

2.3.1 Homomorphic Wavelet approach

In [24], and again in [25], which tested both hard and soft thresholding (Fig. 2.1), a logarithmic transformation is applied to obtain an additive model (though non-Gaussian for small value of L). These early methods, despite the empirical selection of the threshold, show already a clear performance gain w.r.t. spatial-domain adaptive filters, especially for the 1-look images, the most critical case. Many works were proposed to face the problem of threshold selection such as adaptively threshold of the noisy image in [26], or empirical shrinkage in an adaptive fashion [27]. However such all approaches assume no a priori hypothesis on the reflectivity of the scene.

Further improvements are obtained by optimizing the shrinkage parameter through a statistical Bayesian approach. Choosing a MAP approach, an appropriate model of the log-transformed reflectance in the wavelet domain is needed, like the alpha-stable distribution proposed in [28], the normal inverse Gaussian used in [29], or the simpler Cauchy distribution adopted in [30].

Becuase of the alpha-stable distribution [28] does not have a closed-form expression, the estimation of the *pdf* parameters from noisy is hampered and the Bayesian estimator obtained does not have a closed-form. This approach, exploiting the numerically computation to counter the estimates problem, shows a huge increase of the complexity.

The novelty of the work [30] is the simpler way to model the log-transformed wavelet image coefficients. Observing that two special cases of the alpha-stable distribution have a closed-form expressions, the Gaussian and Cauchy *pdfs*, Bhuiyan proposed the simple Cauchy prior, which has the advantage to be symmetric, to have a sharp peak around zero with heavy tails and to have only dispersion parameter to estimate. This prior leads to the derivation of both a MAP and a MMAE (minimum mean absolute error) Bayesian estimators, the latter proving superior in most experiments.

The major inconvenience of usage of the wavelet in an homomorphic way, is that the mean of reconstructed signal shows a bias, due to the mean of the log-transform speckle. In fact, because of the wavelet shrinkage is exploited only in the details subband, leaving unchanged the smoothing version, and the log-transformed speckle has non zero men, the signal after filtering shows a different mean value. A solution to this problem was proposed by Xie *et al.*, [31], which adjusts the mean value adding a further processing step.

2.3.2 Non-homomorphic Wavelet approach

In order to overcome the drawbacks of the homomorphic approach, several authors look to the additive signal-dependent speckle model ([12]) in the wavelet domain. In [32], inspired by [33], a low complexity MMSE estimation procedure is proposed to derive the shrinkage factor for each wavelet coefficient. In [34] a multiscale local coefficient of variation is defined to handle non-stationarities, while [35] proposes a modified ratio edge detector to the same end. In order to deal with scene heterogeneity, being edge information very important to preserve structure during despeckling, in [35] it is proposed a modified ratio edge detector, with the aim to obtain such information through

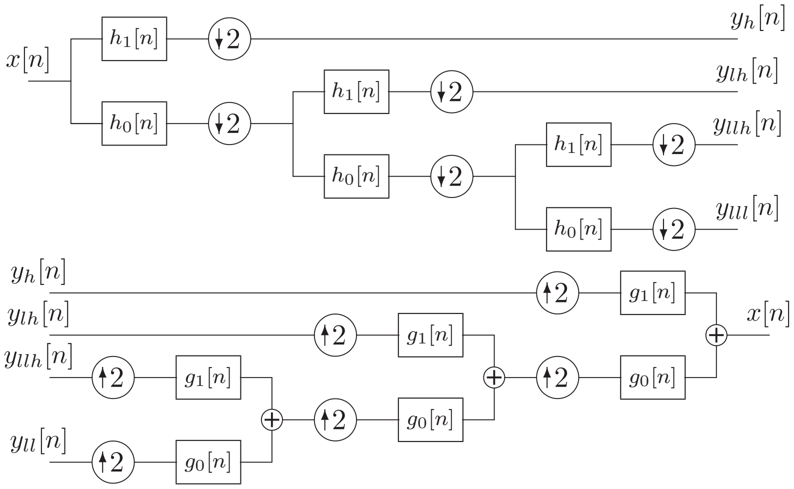

Figure 2.2: Wavelet filter bank.

a lower computational complexity.

In [34], the problem of detecting local non stationarity, to preserve image structure, is addressed defining a multiscale local coefficient of variation in the undecimated wavelet domain. In this context, inspired by [14], an empirical criterion is used in order to reduce the rescaling factor for coefficients in highly heterogeneous areas. In particular, the authors extend MMSE filtering to deal with multiplicative noise and applied to undecimated wavelet frames. In fact, in the image processing community critically subsampled wavelets are preferred in case of redundancy suppression, while in applications such as denoising, a redundancy is considered as a further benefit for processing [36].

The advantages of using undecimated wavelet domain is that dyadic wavelet decompositions, which is an iteration of filtering and downsampling (Fig. 2.2), is not translation invariant [37], so this makes the estimation of non stationary signal and noise variance critical. Moreover when coefficients are rescaled, the aliasing term between two adjacent subband is no canceled in the synthesis stage resulting in annoying artifacts.

Also in this setting can be considered a MAP estimation approach as in [38] where a Gamma distribution is used to model radar reflectivity. In [39] it is assumed that the undecimated wavelet coefficients follow a generalized Gaussian (GG) distribution, with spatially-varying parameters. Indeed, such distribution is characterized by only two parameters compared with such models as beta-complex (Pearson, type IV) distributions [38] and normal inverse Gaussian [29], [40], which have four parameters. Although these models are capable of fitting skewed histograms, they are very complex and the parameters estimation becomes a prohibitive problem.

GG *pdfs* have been already used to globally model the histograms of wavelet coefficients, within a whole subband or frame in [22], [41]. In [39], Argenti *et al.* recall the GG assumption for wavelet coefficients to hold also locally, with space-varying parameters. In particular he explains how the GG parameters of the speckle-free reflectivity and the signal-dependent noise are derived, through the relationships between these moments and the moments of observable noisy variables.

This latter work is further improved in [42] where wavelet coefficients are classified based on their level of heterogeneity, in order to incorporate this information in the filtering procedure. Information about scene heterogeneity is very important because the local stationarity and ergodicity assumptions, to obtain the statistical estimation of parameters, may no longer be verified [15]. In [39], the authors neglect the cross correlation of the reflectivity pixel to have a more simple GG parameters estimation. This assumption is justified in homogeneous areas, but no longer in textured ones. Moreover, in case of extremely heterogeneous areas, like point targets, being the speckle not fully developed, not processing at all could result in a better strategy. Thus Bianchi *et al.* propose in [42] an improvement of the algorithm in [39]. First of all the authors compute and use the exact expression to estimate the parameters of the GG distribution, taking into account also the case of strongly correlated reflectivity.

The wavelet-domain techniques, just as for spatial-domain techniques, try to incorporate some forms of spatial adaptivity in the filtering process in order to better preserve image boundaries and textures. Therefore, the suitable use of contextual information, introduced by non local techniques, keeps being a topic of central importance.

2.4 Non-local techniques

One of the most important innovation of recent years in denoising literature has been the introduction of non-local approach. Non-local filtering represents a complete change of perspective in AWGN denoising, since the “true” value of the current pixel is no more estimated from the pixels closest to it, but from

Figure 2.3: Self-similarities in images

those pixels, located anywhere in the image, which have the most similar context. This approach relies on the observation that most natural images present clear self-similarities as well as SAR images. As it is possible to see in the Fig. 2.3, most patches repeat almost identically over and over in the image. Once these similar patches are identified, they can be exploited to carry out noise filtering.

Non-Local Means

One of the first and most popular non-local denoising algorithm is Non-local Means (NLM) [43], introduced by Baudes and Morel in 2005. In NLM the filtering is carried out, as usual, through the weighted mean of all the pixels in a certain search area; the weight associated with each given pixel, however, depends not on its geometrical distance from the reference pixel but on its contextual similarity with it, measured by the Euclidean distance between the

Figure 2.4: Collection of similar patches.

patches surrounding the selected and the reference pixel. It takes inspiration on the patch-based approach used for inpainting application, proposed by Efros and Leung [44].

The weight $w(s,t)$ defined by comparing two patches B_s and B_t centered respectively around the pixel s and t, is the following:

$$w(s,t) \triangleq exp\left(-\frac{1}{h}\sum_{k}\alpha_k|c_{s,k}-c_{t,k}|^2\right) \tag{2.7}$$

where $c_{s,k}$ and $c_{t,k}$ are the k-th neighbor in the patch B_s and B_t, respectively, α_k define a centered symmetric Gaussian kernel and h controls the decay of the exponential function. The similarity measure is a weighted Euclidean distance over the two windows, well-adapted and robust in the WGN model (Fig. 2.4). It is interesting to note that in [45] the non-local means approach is classified as pointwise. In fact a pointwise estimator provides the estimate for a single point only, the reference pixel in this case.

PPB

NLM has been readily extended to SAR despeckling [46, 47, 48] with suitable modifications aimed at taking into account the problem peculiarities. The Probabilistic Patch-Based (PPB) algorithm [48] is especially interesting, both for its theoretical contribution, with the development of a similarity measure well suited to SAR images, and for the excellent performance on test images.

PPB is a denoising algorithm developed by a more general approach for patch-based denoising in the framework of Weighted Maximum Likelihood Estimation (WMLE). The WMLE has first been applied to image denoising by Polzehl and Spokoiny [49]. Contrary to Polzehl and Spokoiny, in PPB the weights are defined following a statistically patch-based approach both in the case of AWGN and speckle noise. The authors of PPB have proved that the Non-local means algorithm appears as a special case of their algorithm. So they aim to define a suitable patch-based weight to generalize the Euclidean distance based weight used in the Non-local means algorithm, proposing an extension of this concept to non additive WGN models.

In PPB the distance between two patches is based on the speckle distribution model; in short it is due by the probability that the two “clean” patches are equal, knowing the noisy ones. Indeed, recalling the multiplicative model (2.1), and given two noisy observed values $z(s)$ and $z(t)$, the distance is

$$\begin{aligned} d[z(B_s), z(B_t)] = p[z(s), z(t)|x(s) = x(t)] = \\ \int_D p[z(s)|x(s) = \alpha]\, p[z(t)|x(t) = \alpha]\, p(\alpha)\, d\alpha \end{aligned} \tag{2.8}$$

where $x(s)$ and $x(t)$ are the corresponding values of the noise-free signal, defined over the domain D, $p(\cdot)$ indicates a probability density function, and $z(s)$ and $z(t)$ are conditionally independent given x. For more details to this expression we remind the reader to the next chapter.

Furthermore, the authors suggest to refine iteratively the obtained weights (dependent by the distance) by also including the similarity between restored patches. This leads to an iterative algorithm for speckle noise suppression.

An overview on BM3D and SAR-BM3D

NLM has inspired several extensions in the AWGN context, among which the evolution towards a multipoint rather than pointwise filtering, as proposed in the Block-Matching 3D (BM3D) algorithm [50] where the non-local approach is combined with wavelet shrinkage and Wiener filtering in a two-steps process. BM3D can be arguably [45] considered the state-of-the-art for AWGN denoising. It combines three basic idea in a multipoint approach: the non-local approach, the wavelet domain shrinkage and the denoising exploiting in two steps [51].

Each step is composed of three different phases: the grouping, the collaborative filtering and the aggregation. In the first step all similar patches of noisy image are collected in a 3D structure which undergoes a wavelet transform so as to exploit both spatial and contextual dependencies. Once a sparse representation is obtained, an Hard thresholding is used to remove noise components.

Due the multipoint approach, filtered patches can overlap and several estimates of the same pixel are typically obtained. So their weighted average must be computed to reconstruct a basic estimate of the denoised image.

At this point, the second denoising step is carried out: this time the block-matching takes place on a cleaner image (the basic estimate) so as to obtain more reliable matches, a new 3D structure is created, and its empirical energy spectrum is computed to perform Wiener filtering on the transformed noisy 3D structure. Another aggregation concludes the algorithm.

Now the question is how it is possible to carry the winning concepts, exploited in BM3D, in despeckling world? The most trivial solution is to follow an homomorphic approach in order to use directly the technique designed for AWGN case. In spite of its simplicity this solution cannot be considered the best: in fact, especially for images with a small number of looks, this kind of approach does not work well, being the hypothesis of Gaussian noise not satisfied in this case. Furthermore the logarithmic operation changes the data dynamics and, therefore, the distances among patches.

This consideration rises the necessity to project a new non-local technique that works directly on the original image and that is specifically thought for SAR. As PPB can be considered an evolution of Non-local means, specifically thought for speckle noise, our SAR-BM3D method wants to be the evolution specifically thought for speckle noise of the-state-of-art BM3D.

Chapter 3

SAR-BM3D

The despeckling algorithm we propose here can be seen as a SAR-oriented version of BM3D, since we use the same algorithmic structure as the original BM3D but modify most of the individual processing steps in order to take into account the peculiarities of SAR data. Therefore, ideas and tools come from both the AWGN denoising and the SAR despeckling fields. In the following, we outline on a high-level BM3D ideas and algorithmic structure and then we explain the all detailed developments of the proposed algorithm SAR-BM3D [52].

3.1 BM3D

Under some restrictive conditions, the AWGN denoising problem has simple solutions. For example, if the source is wide-sense stationary, with perfectly known statistics, the optimum linear MMSE estimator is the well-known Wiener filter. Unfortunately, real-world images are *never* stationary (the information actually lies in non-stationarities), and their statistics are not easily estimated from noisy sources, which is why more sophisticated techniques are needed.

The wavelet transform (WT) represented a major step forward in this direction. In fact, WT provides a sparse representation of images [53] where large detail coefficients are associated with region boundaries, while small ones contain mostly noise. Therefore, some simple form of coefficient thresholding allows for a strong noise rejection with a good preservation of image details.

Shortly after Donoho first introduced wavelet shrinkage [23], Ghael *et al.* proposed [51] a two-step filtering procedure in the wavelet domain, which will be later reprised in BM3D. The first step is a hard thresholding which provides a basic estimate of the clean image; such an estimate, however, is used only to compute the statistics for an empirical Wiener filtering operating in the transform domain [51] which performs the actual denoising of the original image. Back to Wiener, then, but in the transform domain and with a preliminary hard thresholding that provides the basis for better estimating the relevant statistics.

A further change of perspective came with the non-local filtering approach, recently introduced by Buades *et al.* [43], inspired by image inpainting literature [44] and by early work on neighborhood filters [54]. The non-local approach relies on the observation that most images exhibit clear self-similarities, as most patches repeat almost identically over and over in the image. Once these similar patches are identified, one can carry out the filtering along such patches, wherever they are, rather than in a local neighborhood of the pixel, mimicking a true statistical, as opposed to spatial, filtering.

The BM3D algorithm [50] operates a very effective synthesis of all these ideas. Just like in [51], it works in two steps: the first one uses hard thresholding to build a relatively clean image for estimating statistics, while the second one performs the actual denoising through empirical Wiener filtering in the transform domain. Both steps, however, work not on local neighborhoods, but on groups of blocks drawn from different image locations and collected on the basis of their similarity, in the spirit of the non-local approach. Therefore, the resulting 3D groups are highly redundant allowing for a sparser WT representation and a more effective separation between signal and noise through hard thresholding in the first step; as a further consequence, statistics can be more reliably estimated, and the Wiener filtering of the second step (always working on the 3D groups) turns out to be extremely effective.

We can now summarize, at a very high level, the processing flow of BM3D. The first step, operating on the noisy image, comprises three stages

- grouping: for each reference block, the most similar blocks are located in the image according to a minimum Euclidean distance criterion;
- collaborative filtering: each 3D group undergoes WT, hard thresholding and inverse WT;
- aggregation: all filtered blocks are returned to their original location and contribute with suitable weights to the basic estimate of the image.

The second step comprises the same three stages, with the following differences

- grouping: blocks are located based on the basic estimate provided by the first step;
- collaborative filtering: each 3D group (of noisy blocks) undergoes DCT/WT, *Wiener filtering* and inverse transform;
- aggregation: like in step one.

This minimal summary is meant as a key for going through the rest of the thesis. A detailed description of BM3D, however important for a full understanding of the proposed algorithm, goes outside the scope of this work, and the reader is referred to [50] for more details. Likewise, we neglect some recent variations proposed to improve the performance of the basic algorithm (e.g., [55]) as well as further studies on its application to more specific cases (e.g., [56]).

3.2 Adapting BM3D to deal with SAR speckle

BM3D was developed in AWGN hypotheses, and using it with SAR images, characterized by multiplicative noise, makes little or no sense. Of course, one can always resort to the homomorphic approach, converting the multiplicative noise to additive, and using BM3D on the transformed data, before going back to the original domain. Indeed, this simple approach provides sometimes surprisingly good results, as shown in the experimental section[1]. Nonetheless, the log-transform modifies the dynamics of the data, introducing unwanted artifacts, and the noise remains markedly non-Gaussian (especially for the single-look case) with a sure loss of performance. Therefore, in this work we decided to use the BM3D filtering structure because of its compelling rationale, but also to adapt it to the specific characteristics of the data, modifying the various processing steps so as to take into account the actual statistics of SAR noise. To this end we introduce two major modifications.

First of all, we adapt the criterion used to collect blocks in the 3D groups to the actual data statistics. For each reference block, BM3D looks (in a suitable search area) for those blocks which are closest to the reference in terms of Euclidean distance. In the AWGN setting this makes perfect sense because a smaller Euclidean distance corresponds to a higher likelihood that the two

---

[1] A more sophisticated log-domain version of BM3D has been recently proposed in [57], which however addresses only the case of single-look amplitude images.

signal blocks (without noise) be equal, which is what the collaborative filtering needs. However, once the noise statistics change, as happens with SAR images, the Euclidean distance loses its significance and we need a different *ad hoc* similarity measure in order to keep identifying the signal blocks that are more likely to be equal to the reference one.

Our second modification stems from the same line of reasoning and concerns the collaborative filtering itself. In fact, hard thresholding is a reasonable choice in AWGN, since it is the minimax estimator of the uncorrupted group [23], but this is no longer true with multiplicative noise where a more suitable wavelet shrinkage strategy can be devised. In this work, in particular, we adopt the local linear minimum mean-square error (LLMMSE) solution, discussed in depth in next Section. Together with this “compelling” modification, we introduce a further change consisting in the use of the undecimated WT (UDWT), aimed at obtaining more reliable estimates in the first step, especially needed in the presence of such intense noise. Indeed, by eliminating the decimation step, UDWT guarantees shift-invariance (thus avoiding artifacts such as Gibbs phenomena after thresholding) and provides a larger number of samples for subsequent estimates. On the other hand, UDWT is quite data-intensive and gives rise to correlated coefficients, thus uncoupling optimality in the original and transform domain. Nonetheless, it has been shown experimentally [58], and justified theoretically [59], to provide better results than nonredundant WT, and has already been successfully applied to LLMMSE shrinkage in the case of speckle [34, 60].

3.3 Proposed SAR-oriented modifications in detail

In this section we analyze in some depth the modifications adopted in BM3D in order to deal effectively with speckled SAR images. Under the hypothesis of fully developed speckle, the observed backscattered signal, $z(s)$[2], can be expressed as

$$z(s) = x(s)u(s) \tag{3.1}$$

where $x(s)$ is the noise-free reflectance and $u(s)$ the speckle, in intensity format, characterized by a unitary mean and independent of x. Equation (3.1) can be rewritten in terms of signal plus signal-dependent additive noise $v(s)$,

$$z(s) = x(s) + [u(s) - 1]x(s) = x(s) + u'(s)x(s) = x(s) + v(s), \tag{3.2}$$

---

[2] For notational compactness we use a single argument to indicate spatial location.

It is worth noting that, due to the independence of x and u, and the fact that u' has zero mean, the additive noise v, whose variance depends on x, is zero-mean and appears to be uncorrelated with x. In the following, starting from the above model, and with the further assumptions that both signal and noise are spatially uncorrelated, we will first introduce two new similarity measures, and then two LLMMSE shrinkages in the transform domain respectively for the two steps of the algorithm.

3.3.1 Block similarity measure

The non-local approach can be regarded as an attempt (limited by complexity and data scarcity) to carry out truly statistic, as opposed to spatial, averages. Assuming one is able to collect an arbitrary number of blocks with the same signal component and differing only in the noise realization, one can easily remove most noise (all of it in the limit) with simple filtering operations. Therefore, the block matching phase of BM3D aims at locating the blocks most likely to have the same signal component as the reference which, in AWGN hypotheses, coincide with those having the smallest Euclidean distance from the reference in the data space.

Outside of the AWGN realm, the Euclidean distance is not optimal anymore, but one can follow the same probabilistic principle to devise a new similarity measure based on the actual noise distribution. This is done for example in [61] and in [48] where a function of the fluctuations in the image is used, which represents the likelihood that two observations correspond to the same noise-free scene radiance.

Mathematically, given two observed amplitude values $a(s)$ and $a(t)$, with $a(\cdot) = \sqrt{z(\cdot)}$, it results

$$p[a(s), a(t)|x(s) = x(t)] = \int_D p[a(s)|x(s) = \alpha]\, p[a(t)|x(t) = \alpha]\, p(\alpha)\, d\alpha \tag{3.3}$$

where $x(s)$ and $x(t)$ are the corresponding values of the noise-free signal, defined over the domain D, $p(\cdot)$ indicates a probability density function, and we have assumed $a(s)$ and $a(t)$ to be conditionally independent given x. This expression further simplifies to

$$p[a(s), a(t)|x(s) = x(t)] \propto \int_D p[a(s)|x(s) = \alpha]\, p[a(t)|x(t) = \alpha]\, d\alpha \tag{3.4}$$

if we assume, lacking any prior knowledge, $p(\cdot)$ to be uniform over D.

Considering that for an L-look amplitude SAR image speckle can be modeled [1, 8] by a square-root gamma distribution with order L

$$p(a|x) = \frac{2}{\Gamma(L)} \left(\frac{L}{x}\right)^L a^{2L-1} \exp\left(-L\frac{a^2}{x}\right) \qquad a \geq 0 \tag{3.5}$$

equation (3.4) reads as

$$p[a(s), a(t)|x(s) = x(t)] \propto \int_0^\infty \frac{4L^{2L}}{\Gamma^2(L)\alpha^{2L}} \times \\ \times [a(s)a(t)]^{2L-1} \exp\left\{-\frac{L}{\alpha}\left[a^2(s) + a^2(t)\right]\right\} d\alpha \tag{3.6}$$

with the integral equal to [48],

$$4L\frac{\Gamma(2L-1)}{\Gamma^2(L)} \left[\frac{a(s)a(t)}{a^2(s) + a^2(t)}\right]^{2L-1} \tag{3.7}$$

To translate this result into a manageable block similarity measure we must rewrite equation (3.3) with vectors drawn from the blocks B_s and B_t in place of scalars, and assume again the conditional independency of the observed values given the noise-free signal. Then we define the block similarity measure as

$$\begin{aligned} & d[a(B_s), a(B_t)] = \\ & -\log\Big\{\prod_k p[a(s+k), a(t+k)|x(s+k) = x(t+k)]\Big\} = \\ & -\log\Big\{\prod_k 4L\frac{\Gamma(2L-1)}{\Gamma^2(L)} \left[\frac{a(s+k)a(t+k)}{a^2(s+k) + a^2(t+k)}\right]^{2L-1}\Big\} \end{aligned} \tag{3.8}$$

where $a(B_s)$ is the vector of observed values drawn from block B_s, s is the reference pixel of the block and k is used to scan the whole block. Finally, discarding the constant term, the block similarity measure reduces to [48]

$$d_1[a(B_s), a(B_t)] = \\ (2L-1)\sum_k \log\left[\frac{a(s+k)}{a(t+k)} + \frac{a(t+k)}{a(s+k)}\right] \tag{3.9}$$

where the subscript 1 indicates that this measure is used in the first step.

In the second step, in fact, the similarity measure must take into account the additional information provided by the first step, which is a coarse estimate of the noiseless signal $\hat{x}$. Therefore, inspired by [48], where this approach is used for iterative denoising in a Bayesian framework, we define the similarity measure in the second step as

$$d_2[a(B_s), a(B_t)] = \sum_k \Big[(2L-1)\log\left(\frac{a(s+k)}{a(t+k)} + \frac{a(t+k)}{a(s+k)}\right) + \\ + \gamma L \frac{|\hat{x}(s+k) - \hat{x}(t+k)|^2}{\hat{x}(s+k)\hat{x}(t+k)} \Big] \tag{3.10}$$

where γ weighs the relative importance of the data and (loosely speaking) prior terms. Note that, unlike in [48], there is only one weight to tune, because we are only interested in ranking the blocks based on their similarity with the reference and not in computing any *absolute* measure.

3.3.2 Group shrinkage

The hard thresholding used by BM3D in the first step is a reasonable choice in the AWGN context, but not anymore in the presence of SAR speckle. Therefore, we address the shrinkage problem in the framework of statistical estimation, with the noise model of (3.2), and look for the optimum linear estimator in the minimum MSE sense. It is worth emphasizing that WT and shrinkage take place on each 3D group individually, and hence, in this subsection, the group will be our basic data unit. After the linear wavelet transform, we obtain

$$\mathbf{Z} = \mathbf{X} + \mathbf{V} \tag{3.11}$$

where we have used capital letters for the transformed data, and boldface to indicate the vectors formed by all the coefficients of the group. Under the constraint of linearity, the optimal MMSE estimator is [17]

$$\hat{\mathbf{X}} = E[\mathbf{X}] + (\mathbf{C}_{XZ})(\mathbf{C}_Z)^{-1}(\mathbf{Z} - E[\mathbf{Z}]) \tag{3.12}$$

where $E[\cdot]$ denote statistical expectation, $\mathbf{C}_Z$ is the covariance matrix of $\mathbf{Z}$, and $\mathbf{C}_{XZ}$ the cross-covariance matrix of $\mathbf{X}$ and $\mathbf{Z}$. Since signal and noise are uncorrelated in the spatial domain they remain uncorrelated also after the linear transform, with noise still zero-mean, therefore (3.12) simplifies to [17]

$$\hat{\mathbf{X}} = E[\mathbf{X}] + (\mathbf{C}_X)(\mathbf{C}_X + \mathbf{C}_V)^{-1}(\mathbf{Z} - E[\mathbf{Z}]) \tag{3.13}$$

If we further assume that the covariance matrices are diagonal, the estimation acts separately on each coefficient of the group

$$\hat{X}(i) = E[X(i)] + \frac{\sigma_X^2(i)}{\sigma_X^2(i) + \sigma_V^2(i)}(Z(i) - E[Z(i)]) \tag{3.14}$$

and we obtain a local LMMSE filter, which is indeed an adaptive Wiener filter in the transform domain [32, 33].

The hypothesis that both signal and noise coefficients are uncorrelated is quite reasonable when a wavelet transform is used, since it tends to decorrelate the data, and in fact the local Wiener filter has been used extensively in the AWGN context [51, 62, 63, 64] providing a performance typically superior to that of classical thresholding. Of course, such hypothesis does not hold anymore with the UDWT, which is non-orthogonal and introduces some redundancy among the coefficients. Nonetheless, even in this case such an assumption is typically convenient, as the cost for the imperfect modeling is more than compensated by the opportunity to use a local estimator and by the significant reduction in complexity.

Since the shrinkage is applied only to the coefficients of the detail subbands, which can be reasonably considered to have zero mean, (3.14) becomes eventually

$$\hat{X}(i) = \frac{E[X^2(i)]}{E[X^2(i)] + E[V^2(i)]} Z(i) \tag{3.15}$$

or equivalently

$$\hat{X}(i) = \frac{E[Z^2(i)] - E[V^2(i)]}{E[Z^2(i)]} Z(i) \tag{3.16}$$

The problem now comes down to the estimation of the second order moments in the above formulas. In the literature, working with large images, these quantities are typically computed by means of sliding-window averages running on the various detail subbands of the wavelet transform. In our case, however, we deal with rather small groups (*e.g.,* $8 \times 8 \times 16$ coefficients) which, after an ordinary WT, would be decomposed in tiny detail subbands, making any such estimate totally unreliable. This is why we turn to UDWT for the first shrinkage step, as it provides us with subbands large enough to carry out reliable estimates.

First step

to carry out the estimates required in (3.16), we assume that the second order statistics of the observed signal, given the limited size of the 3D group, are constant over the whole group in the spatial domain, and over each subband in the transform domain. Therefore, we have

$$E[Z^2(i)] = \langle Z^2 \rangle_{\mathrm{SB}(i)} = \frac{1}{|\mathrm{SB}(i)|} \sum_{j \in \mathrm{SB}(i)} Z^2(j) \tag{3.17}$$

where $\langle \cdot \rangle_{\mathrm{SB}(i)}$ indicates average over the subband comprising the i-th coefficient.

As for the noise, this problem was addressed in [34] with reference to the UDWT case, obtaining

$$E[V^2(i)] = \frac{\sigma_u^2}{(1+\sigma_u^2)} \sum_k h^2(k) E[z^2(i-k)] \tag{3.18}$$

where h is the subband equivalent filter, σ_u^2 a known parameter depending on speckle format and number of looks [8], and k spans a 7×7 local window. Adapting the formula to our case we readily obtain

$$E[V^2(i)] = \frac{\sigma_u^2}{(1+\sigma_u^2)} \langle z^2 \rangle_{\mathrm{G}} \tag{3.19}$$

where $\langle \cdot \rangle_{\mathrm{G}}$ indicates the average over the whole group. It is worth observing that the increase in complexity due to the use of an undecimated transform is compensated by the use of subband-wise and group-wise, as opposed to sliding-window, averages.

Eventually we have

$$\hat{X}_1(i) = \max\left(0, \frac{\langle Z^2 \rangle_{\mathrm{SB}(i)} - \frac{\sigma_u^2}{(1+\sigma_u^2)} \langle z^2 \rangle_{\mathrm{G}}}{\langle Z^2 \rangle_{\mathrm{SB}(i)}}\right) Z(i) \tag{3.20}$$

where the subscript 1 indicates first step, and the $\max$ operator accounts for a possible sign inversion due to estimation errors.

Second step

the collaborative filtering in the second step has also a LLMMSE nature with the major difference that now an estimate of the noiseless signal coefficient is already available. As a first consequence, we can use simpler non redundant transforms, thus reducing complexity. In addition, with reference to (3.15), we estimate $E[X^2(i)]$ simply as $\hat{X}_1^2(i)$ where $\hat{X}_1(i)$ is the coefficient computed from the partially denoised signal $\hat{x}_1(n)$ provided by the first step. This amounts to using the empirical Wiener filtering, proposed in [51] for the AWGN context and also used in the original BM3D [50]. Finally, to estimate $E[V^2(i)]$ we assume it is constant over the group, and exploit again the first-step estimate $\hat{X}_1^2(i)$ carrying out an average over the whole group of the difference between the observed coefficient and its noiseless estimate as

$$E[V^2(i)] = \langle V^2 \rangle_{\mathrm{G}} = \frac{1}{|\mathrm{G}|} \sum_{i \in \mathrm{G}} [Z(i) - \hat{X}_1(i)]^2 \tag{3.21}$$

In conclusion the second-step estimate reads

$$\hat{X}_2(i) = \frac{\hat{X}_1^2(i)}{\hat{X}_1^2(i) + \langle V^2 \rangle_{\mathrm{G}}} Z(i) \tag{3.22}$$

3.3.3 Aggregation

To conclude the description of our algorithm let us focus on the aggregation phase. Since a given pixel $x(s)$ can be included in more than one group, and hence estimated several times, each time with a possibly different value, such values must be averaged using suitable weights

$$\hat{x}(s) = \frac{1}{T} \sum_{G \in \mathcal{G}(s)} w_G \hat{x}_G(s) \tag{3.23}$$

Here, $\hat{x}_G(s)$ is the estimate provided from group G through inverse transform, w_G the corresponding weight, $\mathcal{G}(s)$ is the set of all groups comprising $x(s)$, and $T = \sum_{G \in \mathcal{G}(s)} w_G$ is a normalizing factor.

Like in [50] the weights are made to depend on the presumed reliability of the associated group estimate, related in turn to the average noise power of the group after shrinkage. In formulas

$$w_G \propto \frac{1}{\langle V^2 \rangle_{\mathrm{G}} \langle S^2(i) \rangle_{\mathrm{G}}} \tag{3.24}$$

where $S(i)$ is the shrinkage factor for the i-th coefficient of the group. Both (3.23) and (3.24) hold for both steps (we put no subscripts to simplify notation) although the expressions for $\langle V^2 \rangle_{\mathrm{G}}$ and for the shrinkage factors are obviously different.

3.4 Experimental results

In SAR image denoising, given the lack of the original noiseless signal, performance assessment is quite a challenging task. Different indicators have been proposed to measure smoothness of smooth areas as well as sharpness of edges and details, but they are largely empirical, and provide little insight about how to balance image cleanness and preservation of diagnostic information. Therefore, following an approach widespread in the literature [30, 34, 39, 48], we start with experiments carried out on optical images corrupted by simulated speckle, obtaining objective performance figures which allow a sound comparison among different denoising algorithms. Then, in the last part of the Section, we discuss experiments with actual SAR images.

3.4.1 Reference techniques and parameter setting

We compare the proposed technique with three state-of-the-art despeckling algorithms: the spatially adaptive wavelet homomorphic shrinkage algorithm (SA-WBMMAE) [30], the wavelet-based MAP filtering algorithm (MAP-S) [42], and the Probabilistic Patch Based (PPB) nonlocal filter [48]. Such techniques have been chosen because of their competitive performance and (not least) for the availability of software code to run the experiments. Experimental results have in fact been obtained by using the Authors' own code available online, or run by the Authors themselves on our test images. We also include in the comparison two state-of-the-art AWGN techniques used in a homomorphic setting (with mean-bias correction), the AWGN versions of PPB (H-PPB) and BM3D (H-BM3D), which are especially interesting for images with a large number of looks. Finally, we consider also the well-known Frost filter [11] which, although pretty aged, is a *de-facto* standard, included in many image processing software packages, and used routinely by photo-interpreters of military and civil space agencies.

For all these algorithms, if not stated otherwise, the free parameters are set as suggested in the reference papers. As for the proposed SAR-BM3D algorithm, in the first step we use a Daubechies-8 UDWT transform with a three-level decomposition, and fixed groups of dimension $8 \times 8 \times 16$. Just like in BM3D, the computational burden is reduced by using a relatively small search area, 39×39, and by selecting reference blocks only on every third row and column. Similar choices apply to the second step except for the transform, which is a spatial DCT followed by a Haar DWT along the blocks with a maximum-level decomposition, and for the group dimensions that grow to $8 \times$

	Lena			
	L=1	L=2	L=4	L=16
Noisy	12.11	14.89	17.80	23.76
Frost	19.17	23.31	26.33	30.59
SA-WBMMAE	25.06	27.26	29.04	32.40
MAP-S	26.35	28.04	29.78	33.19
PPB	26.71	28.44	29.84	32.68
SAR-BM3D	**27.93**	**29.62**	31.21	34.15
H-PPB	25.26	27.83	29.68	32.86
H-BM3D	26.40	29.18	**31.23**	**34.51**

Table 3.1: PSNR results for Lena.

8×32. Finally, the weight γ in the similarity measure of (3.10) was set equal to 1, which was found experimentally to guarantee a good performance.

3.4.2 Results with simulated speckle

In order to obtain reliable results, we considered a variety of sources, including some general-purpose images commonly used in the AWGN denoising literature, some aerial photographs which better resemble SAR images in terms of scene structure, and a synthetic image, first introduced by Lee in [65], in order to test structure preservation. SAR-like images are obtained by multiplying optical images by simulated white speckle in amplitude format (square root intensity model) [8] with pdf's corresponding to the cases of 1, 2, 4 and 16 looks. All numerical results are obtained as the average over ten different realizations of the noise process.

The performance is quantified by the Peak Signal-to-Noise Ratio,

$$\mathrm{PSNR} = 10 \log_{10} \frac{|x|^2_{\max}}{\mathrm{MSE}} \tag{3.25}$$

where $|x|_{\max}$ is the maximum value admitted by the data format and the mean-square error

$$\mathrm{MSE} = \langle [x(n) - \hat{x}(n)]^2 \rangle \tag{3.26}$$

is computed as a spatial average $\langle \cdot \rangle$, with x and $\hat{x}$ being the original and denoised images, respectively.

In Tab. 3.1 and 3.2 we report results for two[3] general-purpose 512×512-pixel images, Lena and Boat (Fig. 3.1), widely used as benchmark in the de-

---

[3] Numerical results for *all* tested images, as well as all original and denoised versions of the images, are available at http://www.dibet.unina.it/grip/tgrs11_additional_material.zip

	Boat			
	L=1	L=2	L=4	L=16
Noisy	11.77	14.55	17.46	23.42
Frost	18.65	22.58	25.22	28.33
SA-WBMMAE	23.29	25.22	26.84	29.94
MAP-S	23.98	25.43	27.05	30.48
PPB	24.01	25.59	26.96	29.83
SAR-BM3D	**25.50**	**26.94**	28.44	31.43
H-PPB	23.40	25.41	27.00	29.97
H-BM3D	24.49	26.75	**28.58**	**31.74**

Table 3.2: PSNR results for Boat.

noising community, for L=1, 2, 4, and 16 looks. The best PSNR for each case is put in boldface for the sake of clarity. Although the Frost filter does already a good job, with an improvement of several dBs w.r.t. the noisy image, more sophisticated techniques prove definitely superior, especially for the most critical case of $L = 1$ (no multilook), where an additional gain of 6-8 dB is achieved. SAR-BM3D provides consistently the best performance, gaining from 1 to 1.5 dB w.r.t. PPB which looks as the second best. The only exception to this rule is represented by the homomorphic version of BM3D (H-BM3D) which, for large L, is slightly superior even to the proposed dedicated technique. As a matter of fact, the two algorithms based on the homomorphic approach exhibit quite a similar behavior, becoming more and more competitive with increasing L. This is not surprising, however, since the noise in the log image tends to become Gaussian as L increases, in which case a general-purpose AWGN denoising algorithm in the homomorphic setting becomes a perfectly sensible choice. In the absence of multilook, instead, the proposed SAR-dedicated algorithm provides a clear advantage over the homomorphic approach. Fig. 3.2 shows the zoom of the denoised images provided by all algorithms for Lena with $L = 1$. It is clear that strong noise reduction comes at the price, in general, of some loss of details, most notable in the PPB image. SAR-BM3D and H-BM3D seem to offer the best compromise between these contrasting needs, but the latter also introduces a number of pointwise artifacts which severely degrade the image quality.

Tab. 3.3 gives results for a 512×512-pixel section of an aerial photo showing a prevalently urban scene in the city of Naples (Italy) (Fig. 3.1). The general behavior of the PSNR is quite similar to that of the previous experiments, except for the gap between SAR-BM3D and the reference techniques

(a)Lena (a)Boat (b)Napoli

Figure 3.1: Original images used in the experiments.

	L=1	L=2	L=4	L=16
Noisy	14.29	17.07	19.98	25.94
Frost	20.36	23.52	25.16	26.41
SA-WBMMAE	22.09	23.42	24.79	27.73
MAP-S	22.09	23.45	25.03	29.09
PPB	21.37	22.64	24.34	28.14
SAR-BM3D	**23.56**	**25.02**	**26.63**	**30.09**
H-PPB	19.61	22.13	24.42	28.49
H-BM3D	22.92	24.69	26.37	29.96

Table 3.3: PSNR results for Napoli.

which grows slightly larger. It is worth taking a closer look, instead, at the zoom of denoised images shown in Fig. 3.3. Here, given the wealth of fine details in the original, the smoothing provided by some filtering techniques is particularly annoying, with many individual objects, both cars and boats, merged together or even lost in the background. SAR-BM3D instead, and to a lesser extend H-BM3D and PPB (with a modified setting proposed by the Authors) provide an acceptable balance between smoothing and detail preservation. The latter two, however, introduce again very visible and annoying artifacts. To better substantiate this claim, Tab. 3.4 provides results also in terms of the edge-preservation index β proposed in [28], obtained as the correlation coefficient between the high-pass versions of original and filtered images. Even though this index is largely empirical, and hence should be considered with some reservation, it speaks very clearly in favor of SAR-BM3D and H-BM3D, with all other techniques, including both versions of PPB, lagging far behind.

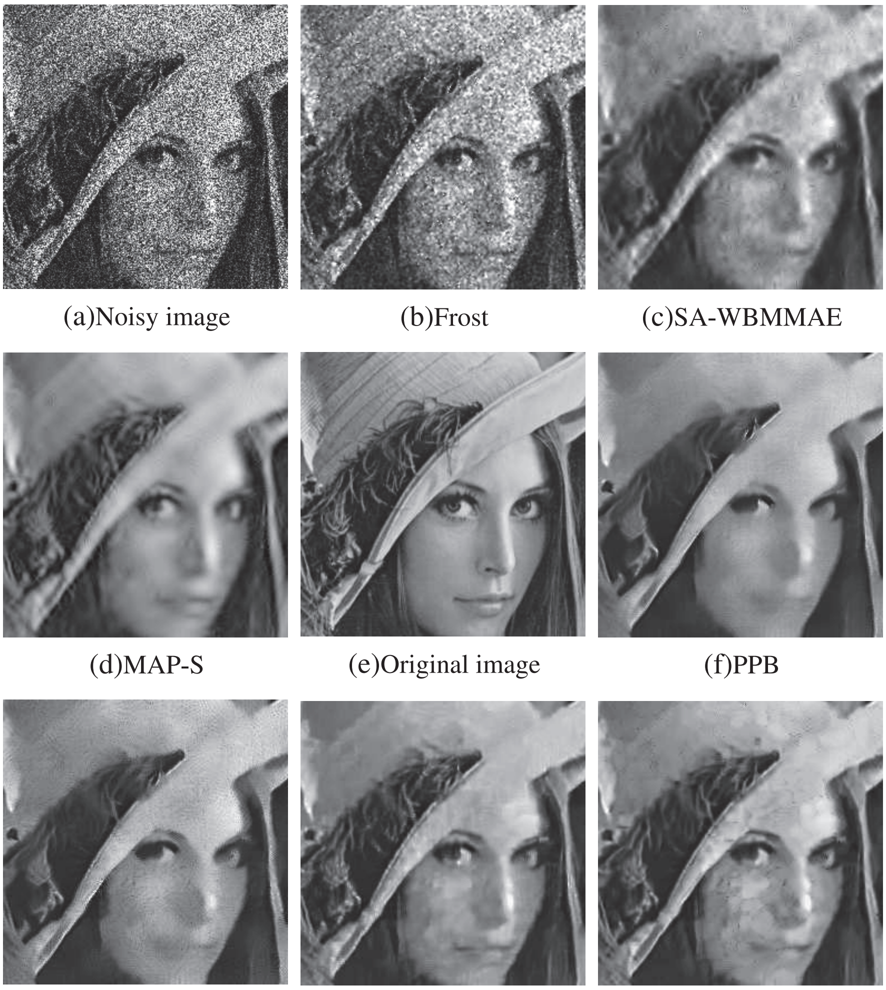

(a)Noisy image (b)Frost (c)SA-WBMMAE

(d)MAP-S (e)Original image (f)PPB

(g)H-PPB (h)SAR-BM3D (i)H-BM3D

Figure 3.2: Lena, L=1: zoom of all filtered images.

Tab. 3.5 and 3.6 finally presents results for the synthetic 256×256-pixel Target image, reported for the first time in [65], which contains points and strips of increasing dimensions. The point targets have size of 1×1, 3×3, and 5×5 pixels, while the strip width goes from 1 to 13 pixels in 2-pixel increments. All target pixels have value 120, while the background pixels have value 60. In terms of PSNR, the most significant difference w.r.t. previous

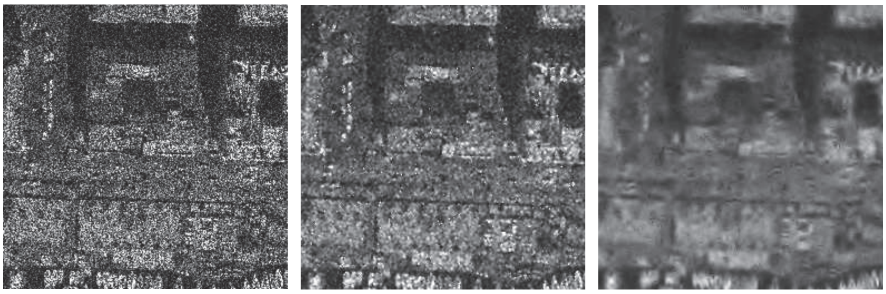

(a)Noisy image (b)Frost (c)SA-WBMMAE

(d)MAP-S (e)Original image (f)PPB

(g)H-PPB (h)SAR-BM3D (i)H-BM3D

Figure 3.3: Napoli, L=1: zoom of all filtered images.

experiments is the larger gain of the BM3D-based techniques over the others. This is probably due to the block-wise processing used in BM3D, which allows to treat coherently neighboring pixels. Filtered images are shown in Fig. 3.4. To test feature preservation, we decided to process them with a simple detector (a gaussian filter followed by a threshold operator), declaring the detection of a target whenever an above-threshold region superimposed the target. Results,

	L=1	L=2	L=4	L=16
Noisy	0.259	0.360	0.484	0.744
Frost	0.350	0.463	0.505	0.517
SA-WBMMAE	0.346	0.465	0.559	0.745
MAP-S	0.287	0.392	0.536	0.820
PPB	0.340	0.468	0.594	0.788
SAR-BM3D	**0.487**	**0.603**	**0.706**	**0.857**
H-PPB	0.285	0.450	0.599	0.801
H-BM3D	0.445	0.590	0.698	0.855

Table 3.4: β index for Napoli.

	L=1	L=2	L=4	L=16
Noisy	17.68	20.48	23.39	29.34
Frost	24.39	28.15	30.44	32.71
SA-WBMMAE	28.20	29.75	31.13	35.06
MAP-S	28.95	30.31	32.00	36.89
PPB	30.06	32.74	35.48	40.31
SAR-BM3D	**32.51**	**36.30**	**39.80**	**45.67**
H-PPB	28.07	31.33	34.47	39.58
H-BM3D	30.79	35.23	38.59	45.05

Table 3.5: PSNR and detection results for Target. Detection results are in terms of average number of identified features (over ten realizations) of the single-look image.

in terms of number of detected features (over ten realizations) in the single-look case, are reported again in Tab. 3.6, and confirm what visual inspection also suggests, namely, that all filters behave about equally well on point targets (lost) and bars (saved), but only SAR-BM3D and Frost save all 5×5 and quite a few 3×3 targets, with the latter generating however an inordinate amount of false alarms (F.A.).

3.4.3 Results with actual SAR images

For this set of experiments we considered five single-look and one 6-look TerraSAR-X images in amplitude format taken over Rosenheim (Rs) (Germany) and Toronto (Tr). Fig. 3.5 shows 512×512-pixel sections drawn from such images covering heterogeneous sceneries: urban areas, fields, woods, a lake. For these images we computed the ENL (Equivalent Number of Looks),

	bars	5×5	3×3	1×1	F.A.
Noisy	–	–	–	–	–
Frost	6.8	7	7	3.7	~ 100
SA-WBMMAE	6.0	7	1.4	0.2	~ 10
MAP-S	6.7	6.8	2.4	0.5	~ 10
PPB	5.6	3.4	0	0	0
SAR-BM3D	6.2	7	2.9	0	0
H-PPB	5.3	2.4	0	0	0
H-BM3D	6.3	4.6	1.0	0	~ 10

Table 3.6: Detection results for Target, L=1. Detection results are in terms of average number of identified features (over ten realizations) of the single-look image.

a standard parameter widely used in the remote sensing community which measures the speckle reduction in homogeneous areas. Once selected an apparently homogeneous region in the image, like those in the white boxes in Fig. 3.5, the ENL is computed as

$$\mathrm{ENL} = \mu_{\hat{x}}^2 / \sigma_{\hat{x}}^2 \tag{3.27}$$

with $\mu_{\hat{x}}^2$ the average intensity of the selected area and $\sigma_{\hat{x}}^2$ its variance. Larger ENL values indicate stronger speckle rejection and, consequently, an improved ability to tell apart different gray levels. Tab. 3.7 reports the ENL values for the proposed and reference algorithms. Results are quite consistent, indicating PPB[4] by far as the technique with the strongest speckle rejection ability, followed by H-PPB, MAP-S, SAR-BM3D and the others. On the other hand, this is immediately obvious by visual inspection of results, like those for the Rosenheim 3 image[5] whose filtered versions are shown in Fig. 3.6. Although the PPB image looks more pleasant than the others, and is probably more helpful to gain a quick insight of the scene, it presents widespread artifacts resembling watercolor strokes. Indeed, SAR-BM3D seems to be the only technique which guarantees a significant noise reduction without introducing some kinds of artifacts. However, with neither the noiseless image nor an expert interpreter, it is difficult to decide whether such artifacts imply any loss of details.

---

[4] In the case $L = 6$ (low-resolution images) the parameter setting is the same used for Naples as indicated by the authors.

[5] Again, detailed results for all images are available at http://www.dibet.unina.it/grip/tgrs11_additional_material.zip

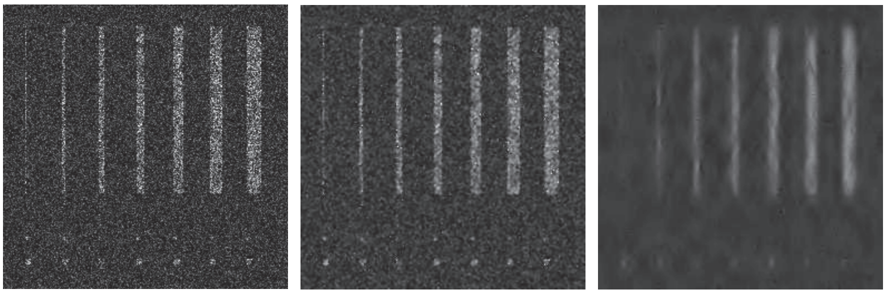

(a)Noisy image (b)Frost (c)SA-WBMMAE

(d)MAP-S (e)Original image (f)PPB

(g)H-PPB (h)SAR-BM3D (i)H-BM3D

Figure 3.4: Target, L=1: all filtered images.

Some help comes from the analysis of ratio images obtained, as proposed in [1], as the pointwise ratio between the SAR original z and denoised $\hat{x}$ images

$$R = z/\hat{x} \tag{3.28}$$

Given a perfect denoising, that is $\hat{x} = x$, the ratio image should contain only speckle, possibly with the expected statistics. On the contrary, the presence

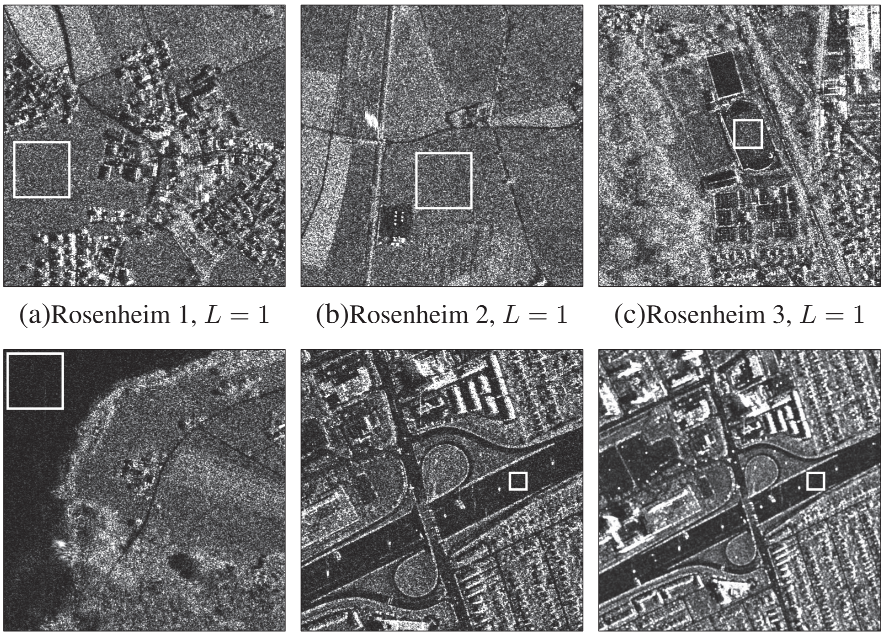

(a)Rosenheim 1, $L = 1$ (b)Rosenheim 2, $L = 1$ (c)Rosenheim 3, $L = 1$

(d)Rosenheim 4, $L = 1$ (e)Toronto, $L = 1$ (f)Toronto, $L = 6$

Figure 3.5: Terra SAR-X images (©Infoterra GmbH).

of geometric structures or details correlated to the original image indicates that the algorithm has removed not only noise but also some information of interest. Fig. 3.7 shows the amplitude ratio images, scaled by a factor 100 corresponding to the denoised images of Fig. 3.6. The Frost ratio image presents visible traces of the man-made structures, denouncing an unwanted smoothing of sharp boundaries, and similar traces, although weaker, are also present for SA-WBMMAE and MAP-S. The PPB and H-PPB ratio images exhibit different patterns depending on the different areas of the scene, though not marked by linear structures, showing again a dependence on the original SAR image. In SAR-BM3D and H-BM3D ratio images, finally, there is no trace of man-made structures nor any obvious pattern.

Regarding the ratio statistics, the expected value is often used in the SAR literature to test the level of bias introduced by the denoising process. Since the considered techniques are designed to preserve the mean of backscattered intensity, the expected value of intensity ratio should be equal to one [1]. The considered algorithms exhibit averages from a minimum of about 0.75 for ho-

	Rs 1	*Rs 2*	*Rs 3*	*Rs 4*	*Tr L1*	*Tr L6*
Noisy	0.95	0.98	0.90	0.94	0.91	7.43
Frost	3.57	3.80	3.05	3.71	3.39	14.66
SA-WBMMAE	3.08	3.05	2.36	2.29	2.79	9.63
MAP-S	14.55	18.56	5.73	18.56	6.70	12.86
PPB	43.01	47.04	19.79	51.24	66.59	15.35
SAR-BM3D	6.75	8.03	4.84	7.78	7.76	11.99
H-BM3D	3.62	3.27	2.76	3.16	3.79	8.58
H-PPB	6.56	4.37	3.85	3.56	7.48	8.89

Table 3.7: ENL for real SAR images.

momorphic methods through 0.89 for SAR-BM3D, to a maximum of 0.92 for PPB. Small values indicate a tendency to "follow" the noise, and hence perform a lighter filtering, but all observed values are reasonably large. Very likely, this is a consequence of the speckle affecting TerraSAR-X images, which does not match the hypotheses of the theoretical model. Indeed, no such polarization is observed in the simulated images for any considered algorithm.

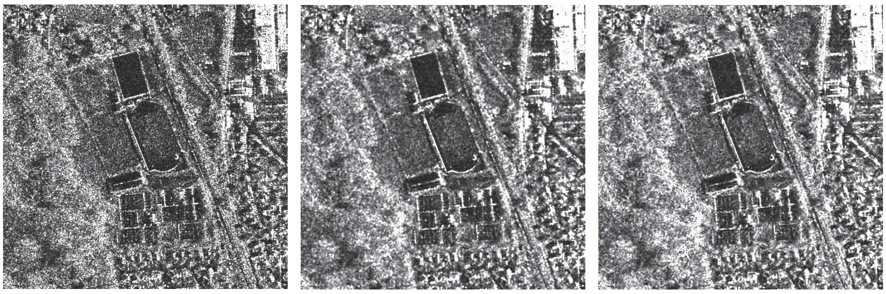

(a)Original SAR image (b)Frost (c)SA-WBMMAE

(d)MAP-S (f)PPB

(g)H-PPB (h)SAR-BM3D (i)H-BM3D

Figure 3.6: Rosenheim 3: all filtered images.

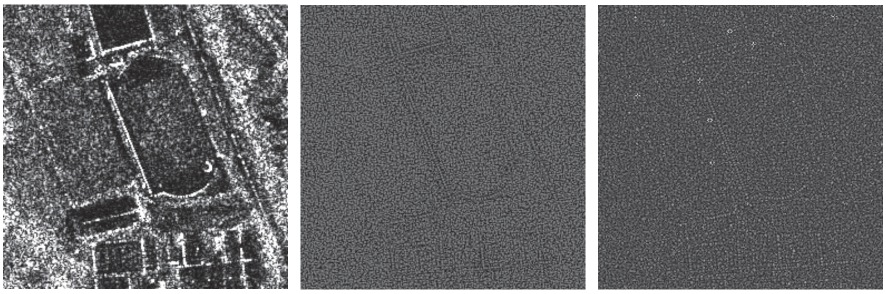

(a)Original SAR image (b)Frost (c)SA-WBMMAE

(d)MAP-S (f)PPB

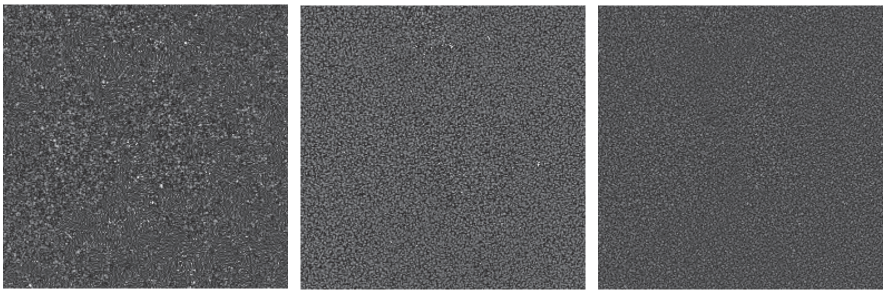

(g)H-PPB (h)SAR-BM3D (i)H-BM3D

Figure 3.7: Zoom of enhanced ratio computed for the various techniques.

Chapter 4

Measuring SAR despeckling performance

Donwstream of the experimental analysis exploited in chapter 3 on the simulated speckle corrupted images, the only ones reliable in literature to compare despeckling techniques, we address the problem of quality assessment on the SAR images. In fact, on real SAR image neither parameters nor measures are exhaustive to describe results of a despeckling processing. In this chapter we outline guidelines to obtain, provided despeckling techniques and simulated SAR images, an objective comparison with the state-of-the-art.

4.1 Common approach to despeckling assessment

Image despeckling has been an active field of research for almost thirty years: many algorithms exploiting powerful tools and advanced signal processing techniques have been proposed, so as result better and better performance have been achieved. However quality assessment is still an open and relevant issue in SAR despeckling. In fact, generally in all denoising applications the uncorrupted reference image, which is the target of the processing, is not known. So far, if we suppose to know exactly the characteristics and the statistical model of the noise, it is possible to simulate it and exploit a managed experimental analysis, corrupting clean images. This is the common and reliable approach used in literature. Obviously this method as realistic and correct as the assumption to know exactly the model of the speckle is verified. Due these statements when we apply despeckling techniques to SAR images we can only do a comparison by visual inspection or exploiting some partial parameters very common in the SAR literature. At this regard the most common parameter is the ENL, which as we shown in the previous chapter, gives only information about the speckle reduction in flat areas. Over the years many authors have dealt with this problem, developing empirical measures such as simply edge detector, statistics of ratio image and so on, all applied on the SAR and filtered images, such as we have done in chapter 3. Nowadays, neither objective and exhaustive parameters to evaluate performance are available, nor a simple set of benchmark images which allows for a clear evaluation of algorithms on SAR images has been found.

These considerations motivate us to provide some agreeable guidelines for performance assessment of despeckling techniques together with insightful experimental results on some state-of-the-art algorithms.

4.2 Proposed approach: objective assessment

Before to go into more technical details, we want to outline the proposed approach, describing what does it mean saying that we will propose an objective performance assessment. Here we want to give an answer to the question "What is the criterion to choose the best despeckling technique?". It is clear that the answer is " It depends on the specific application". In fact, in some applications such as military ones the users is the human eye: *i.e.* human experts analyze these images in order to extract useful information; in other applications the user is an automatic system which performs segmentation or classification. Thus the effectiveness of a given despeckling algorithm should be measured by evaluating the success of the subsequent processing tasks by objective metrics. Actually this approach seems to be very difficult and impractical, because of the results depends not only on the processing but also on the implementation of the algorithms in downstream and on the experience of the human experts, which is however of relevant importance, but has to be joined by a systematic and more objective approach.

Due this conditions, in order to define quantitative measures a reference noise-free image is needed: the availability of this kind of image is a prerequisite for a filter performance analysis based on a comparison between the filtered images and the speckle-free ones. In fact, at least in principle, the filter should remove all the noise affecting the data, and this ability can be tested only if a noise-free image is available. Given this image, one can compute the currently used measure distortion such as the common mean-square error (MSE) and related quantities like the signal-to-noise ratio (SNR) or the peak

SNR (PSNR), up to most recent measures like the structural similarity (SSIM) which tries to provide more meaningful information about the closeness of two images. However, even the definition of a SAR image without speckle is a non-trivial issue. While in classical signal theory the noise is described as a disturbing signal distorting the originally noise-free one, in the SAR case the speckle is a characteristic of the original signal: hence, the speckle-filtered image is a distorted version of the original one. As we said the most common approach is to use an optical reference which approximates the SAR one. But if we compare an optical reference with a “SAR reference” (a SAR image), we can observe physical and statistical differences. In fact, under a physical point of view optical and SAR images differ wildly for operational wavelengths, resolution, imaging modalities and so on. More important, they differs also for the statistics, for dynamic, typical gray-level distribution, spatial correlation and power spectral density.

So we appeal to the simulative approach, which brings the problem of the definition of the clean reference SAR image. An interesting hint comes from the despeckling literature, where the more common performance measure, the equivalent number of looks, suggests that the goal of any despeckling technique is to obtain the infinite-look version of the image under analysis. Ideally, if we were able to collect an arbitrarily large number of SAR images of the same scene, taken with the same system parameters and in the same conditions, we could carry out a multilook with an arbitrarily large number of looks L, without resolution loss. We can therefore consider as clean reference the limit of this image as L grows towards infinity. Once defined the SAR reference, assuming to know the region that we want describe: *i.e.* 3D geometry, electromagnet features, and to reproduce the capture processing, we are able to reproduce an image, which is with a very good approximation of a SAR image.

4.2.1 SARAS images

Here we introduce the simulation framework which allows the generation of a wide set of canonical SAR images, called SARAS by the name of the simulator. These images are used as a meaningful test-bed in order to define objective quality measures and assess the performance of the despeckling techniques. The SARAS simulator is based on sound geometrical and electromagnetic models for the evaluation of the reflectivity function of the scene and on a model for the transfer function of the system for the evaluation of the SAR raw signal. These models are not dependent on the used despeckling technique, thus allowing an objective comparison of the selected filtering techniques. Following, we briefly outline the models used for simulation and the simulated test cases.

Simulation procedure

Considering the SAR as linear time invariant (LTI) system, as we shown in chapter 1, the complex raw signal obtained is

$$i(a',r') = \int\int \gamma(a,r)h(a-a',r-r';r)dadr \tag{4.1}$$

where a and r are independent space variables respectively for azimuth and range, $\gamma(a,r)$ is the reflectivity function of the scene and $h(a'-a,r'-r;r)$ the unit impulse response of the SAR system [1]. To evaluate the reflectivity function are used electromagnetic scattering models which provides a solution function of the sensor and surface parameters. First of all, the description of the macroscopic aspects of the surface at the scale of the sensor resolution is required: this is accomplished providing as input to the simulator a digital elevation model (dem). The behavior of the dem is then approximated using a two scale model [66], i.e. using plane facets, over which a microscopic random roughness is superimposed.

This random roughness can be described using different parameters resulting from the introduction of different models for the geometry of the surface [67]: here, when a natural terrain is considered (i.e., in the first four test cases) the roughness is supposed to be effectively described through a fractal process. Conversely, in the case of the isolated building, when the surface surrounding the building is assumed to be man-made (e.g. asphalt), the roughness is described through classical parameters, the height standard deviation and the correlation length. Finally, in order to complete the description of the surface also the relative dielectric constant ϵ and the conductivity σ $[S/m]$ of the observed surfaces are necessary as input to the simulator. The reflectivity function is evaluated in a ground range-azimuth reference system and then projected it in the sensor-centered slant range-azimuth reference system.

Once this transformation is performed, the obtained reflectivity function can be filtered according to the impulse response of the SAR system, providing as output the raw signal as shown in (4.1). In order to compute the impulse response the radar parameters are needed: the wavelength of the incident field, the resolution of the sensor, the polarization, and so on. After focusing, the obtained raw signal provides the final simulated SAR image.

As regard the speckle phenomenon, it is accounted for thanks to the two scale model introduced above for the imaged surface. In this kind of approach the spatial scales smaller and larger than the resolution one are handled differently: in particular, the signal macroscopic behavior is accounted for through the computation of the scattering from plane facets locally approximating the considered surface, assuming that the electromagnetic parameters are known. The microscopic behavior, which determines the presence of speckle, is accounted for through a statistical model: in particular, assuming that the speckle can be considered as fully developed [1], the amplitude value obtained for each facet is multiplied by a particular realization of a Rayleigh random variable. Notice that the inclusion of speckle is performed before the SAR impulse response filtering: in this way also the signal speckle component is filtered according to the system impulse response. This kind of speckle simulation approach allows to obtain the correct spatial properties for the simulated image: this is not possible using speckle simulation techniques based on the multiplication of the desired statistics on a pixel basis over the final simulated image [68].

As we mentioned above, the definition of SAR images with no speckle is not straightforward: if we define them as images whose macroscopic features are not affected by the presence of speckle, they can be seen as SAR images with an infinite number of looks. Usually, when we refer to multilook procedures we refer to some kind of spatial averages, which reduce speckle effects but, in turn, also imply a decrease in the resolution of the image. Besides, a real multilook performed starting from a large set of independent images of the same zone is very difficult to obtain in practice. However, thanks to the introduced simulator we can obtain a SAR image presenting a finite but very large number of looks: in fact, it is possible to obtain it as the average of a large number of independent images relevant to the same input dem. In particular, here, the speckle-free reference images were obtained averaging 512 independent intensity images. Through the above described framework we are able to provide a wide set of simulation products, spanning from the reflectivity function to the Single Look Complex (SLC) image. In this analysis we are interested in intensity images, i.e. the square modulus of the SLC image, which is usually simply referred as SAR image.

Analyzing this product significant features of the observed scene can be visually inspected and effectively processed in order to retrieve significant information. Value added products, presenting further elaborations (e.g. geocoding) are available directly from data providers. However, only the use of

SLC data ensures a complete knowledge of the image characteristics, allowing their accurate statistical description. In fact, in the value added products non-controllable distortions and artifacts can be introduced during the processing. In the following, the set of simulations is presented: the elaboration is intended to provide SLC data and, in particular, the considered despeckling techniques are applied on intensity images.

Test cases

As we said above, we do not use complex simulated scene, but test cases accurately chosen because of their ability to effectively model significant canonical features present in SAR images. In particular, we have selected five test cases introduce following:

- homogeneous area with constant electromagnetic parameters;
- four adjacent homogeneous areas with different electromagnetic parameters presenting returns of different intensity: this case models the presence of discontinuities in SAR signals and can be used to test the performance of the considered techniques with regard to the preservation of edges;
- an image of a canonical fractal digital elevation model (dem) with constant electromagnetic parameters. This case models the presence of texture on SAR images;
- a corner reflector in an homogeneous background, which models the presence of a target to be detected;
- an isolated building on an homogeneous background: this case is mainly used to test whether the considered techniques preserve the radiometric characteristics of the multiple reflection contributions over an urban area [69],[70].

The first four cases are simulated with sensor parameters typical of the ERS sensor, which provide images with ground range resolution $y = 19.9m$ and azimuth resolution $a = 4m$. In the last case, the Cosmo SkyMed high resolution sensor parameters ($y = 3.6m$ and $a = 2.6m$) have been used in order to ensure a resolution adequate for the identification of a typical building. The first test case is obtained simulating a flat surface presenting a microscopic

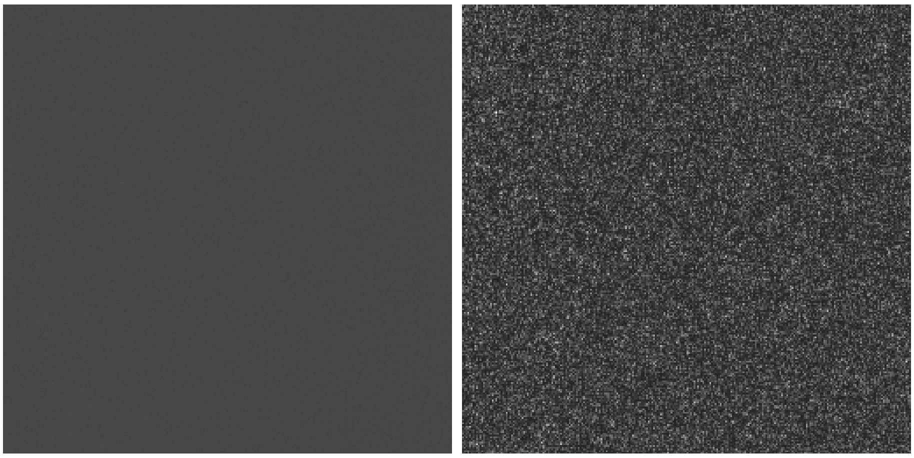

(a)Without speckle (b)With speckle

Figure 4.1: Homogeneous image.

roughness and electromagnetic parameters $\epsilon = 4$ and $\sigma = 0.001$ S/m. The resulting images, without and with speckle, are in Fig. 4.1[1].

The second test case is obtained simulating a flat surface presenting a microscopic roughness equal to that of the previous case and electromagnetic parameters varying in four regions of the image, as shown in Fig. 4.2. If we call the four part from top to bottom and left to right P_1, P_2, P_3, P_4, the electromagnetic parameters are $\epsilon = 4$ and $\sigma = 1$ S/m, $\epsilon = 16$ and $\sigma = 1$ S/m , $\epsilon = 4$ and $\sigma = 0.001$ S/m, $\epsilon = 8$ and $\sigma = 0.001$ S/m, respectively.

The third test case is obtained simulating a SAR image relevant to a canonical natural surface, modeled through the artificial canonical fractal dem, obtained using the Weierstrass-Mandelbrot fractal function, shown in Fig. 4.3, [67]. Note that in this case, due to the presence of a macroscopic topography, some considerations about speckle generation are in order. In the previous cases, due to the fact that the considered surfaces were macroscopically flat, no significant geometrical distortion was present on the final simulated amplitude image. The considered simulator provides speckled images generating independent Rayleigh random variables and multiplying them by the amplitude value of the backscattered field evaluated in each ground range resolution cell [66]. In this way, we are assuming that the statistics for each resolution

---

[1] In the following we visualize all the images in amplitude format (square root intensity) considering the dynamic of the SAR image (the noisy version).

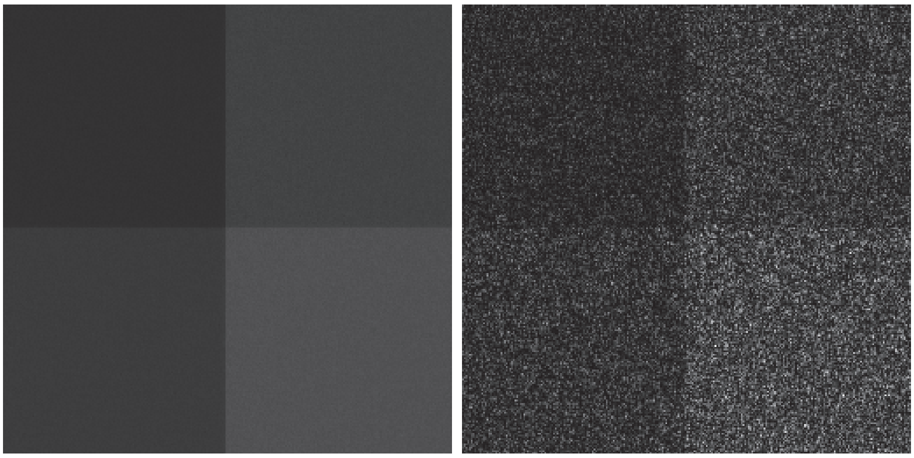

(a)Without speckle (b)With speckle

Figure 4.2: Edges image.

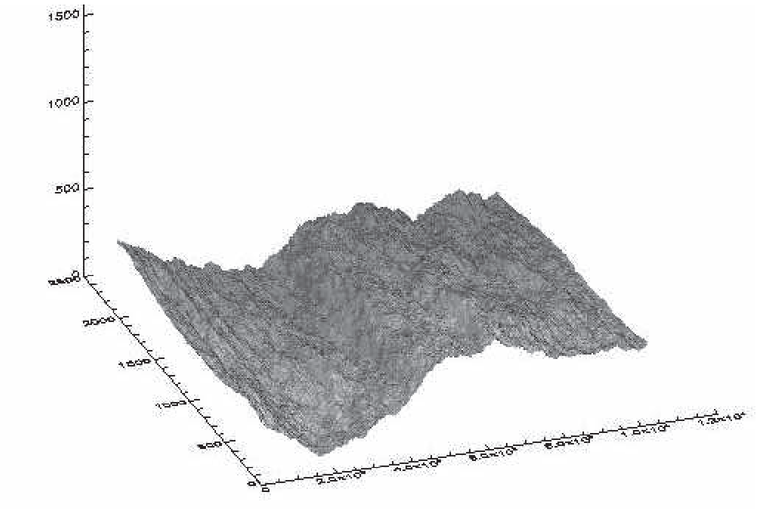

Figure 4.3: Dem as input for the simulations.

cell are those relevant to the fully developed speckle, i.e. a Rayleigh amplitude distribution. This is true also for the statistics of a homogeneous area whenever a flat surface is considered, because the change in the reference system

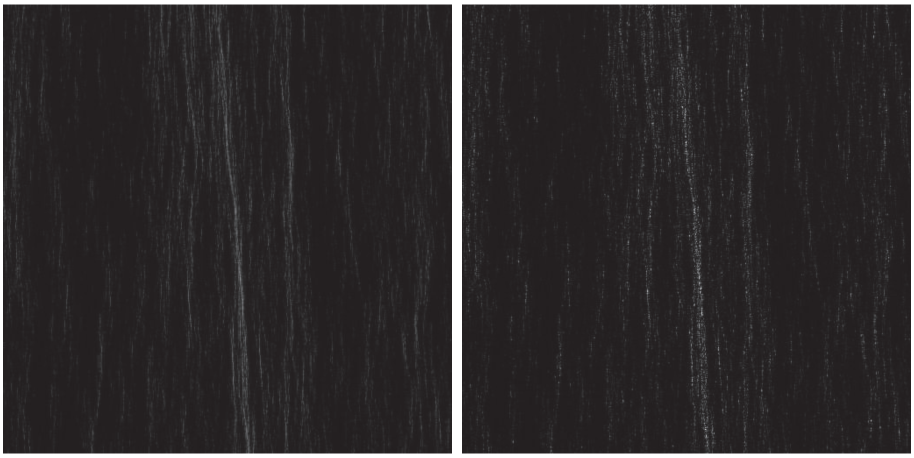

(a)Without speckle (b)With speckle

Figure 4.4: Dem image.

from the ground range-azimuth one to the slant range-azimuth one does not imply significant distortions (apart from the near range-far range effect); conversely, when a significant topography is present on the imaged surface, the change in the reference system implies geometrical distortions, thus modifying the speckle statistics. In fact, the occurrence of foreshortening and layover implies that more than one ground range resolution cell are mapped into one slant range resolution cell. This means that the ratio between the speckled and speckle-free intensity images generated by the SARAS simulator does not provide necessarily a Rayleigh distributed image. The obtained simulated images are shown in Fig. 4.4.

The fourth test case (Fig. 4.5) is obtained modifying the value of a pixel at the center of the reflectivity function in order to model the behavior of a corner reflector: the pixel value is posed $40dB$ above the mean value of the image.

The last test case is obtained simulating the presence of an isolated building over an homogeneous background. In this case the observed surface is modeled as a random rough surface described through the standard deviation of the height, $h = 0.02m$, and the correlation length, $lh = 0.07m$. The building is modeled as a parallelepiped with square plant of $40x40m^2$ and height of $20m$ and is placed with one wall parallel to the line of flight of the sensor (Fig. 4.6). The electromagnetic parameters used for the terrain and the building are the same and are $\epsilon = 4$ and $\sigma = 0.001$ S/m. The simulated images are

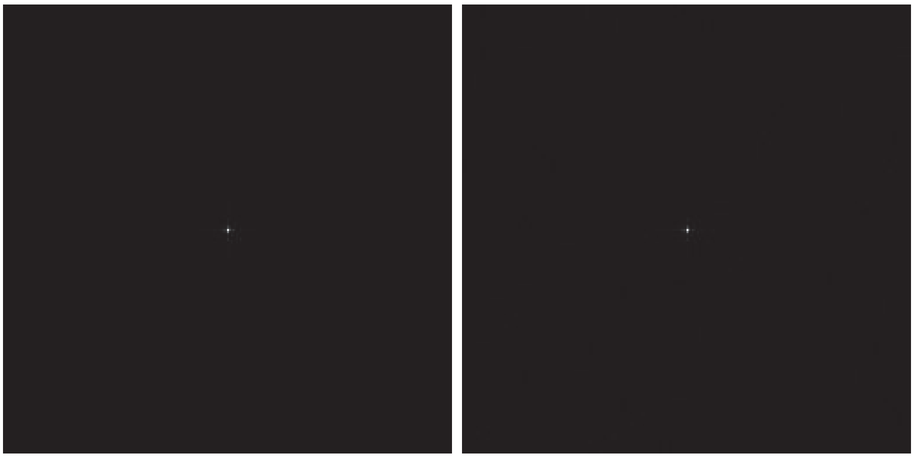

(a)Without speckle (b)With speckle

Figure 4.5: Corner reflector image.

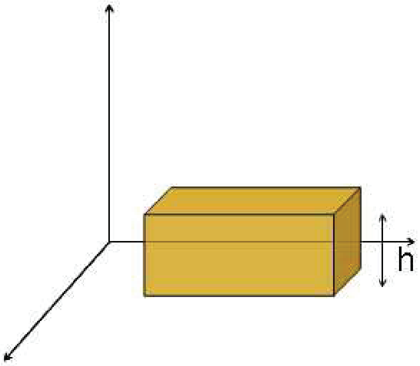

Figure 4.6: Building.

shown in Fig. 4.7.

4.3 Analysis of simulated test cases

In this section we describe in detail the more relevant and interesting measures used in each canonical case and discuss experimental results. For each case we compare performance for the despeckling techniques shown in chapter 3.

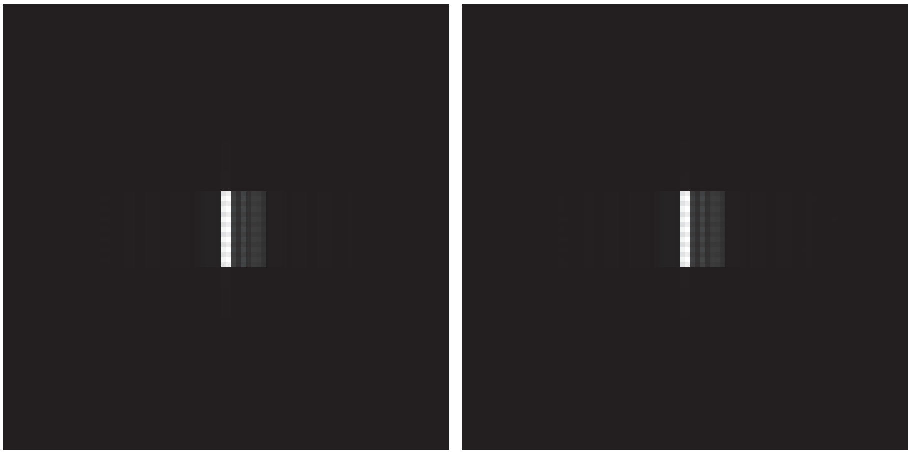
(a)Without speckle (b)With speckle

Figure 4.7: Building zoomed image.

We compare SAR-BM3D with the spatially adaptive wavelet homomorphic shrinkage algorithm (SA-WBMMAE) [30], the wavelet-based MAP filtering algorithm (MAP-S) [42], and the Probabilistic Patch Based (PPB) nonlocal filter [48], all described in chapter 2. We also include in the comparison H-PPB and H-BM3D, the homomorphic version of PPB and BM3D respectively. Finally, we consider Frost filter [11] which is usually included in many image processing software packages.

4.3.1 Homogeneous image

Although homogeneous one could seem a trivial case, it is one of the most relevant because it puts in evidence the performance of different algorithms when dealing with pure speckle reduction, which is already a not simple task. The natural parameters chosen in this case fall on the ENL, computed as

$$\mathrm{ENL} = \mu_{\hat{x}}^2 / \sigma_{\hat{x}}^2 \tag{4.2}$$

and on the signal to noise ratio (SNR), defined as

$$\mathrm{SNR} = 10 \log_{10} \frac{\sigma_x^2}{\mathrm{MSE}} \tag{4.3}$$

where σ_x^2 is the variance of the data and the mean-square error

$$\mathrm{MSE} = \langle [x(n) - \hat{x}(n)]^2 \rangle \tag{4.4}$$

	Homogeneous	
	SNR dB	ENL
Noisy	-26.10	0.99
Frost	-19.40	4.52
SA-WBMMAE	-11.78	32.42
MAP-S	-6.42	**120.41**
PPB	**-6.37**	119.36
SAR-BM3D	-7.36	90.69
H-PPB	-10.85	47.31
H-BM3D	-11.23	47.25

Table 4.1: SNR and ENL results for homogeneous.

is computed as a spatial average $\langle\cdot\rangle$, with x and $\hat{x}$ being the original and denoised images, respectively. These measures give objective information about the speckle reduction. As it is proved by the results in tab 4.1 better performance are achieved by the PPB and MAPS algorithms, which provided the best SNR and ENL. They are readily followed by SAR-BM3D. Even though there is more than one method giving quite satisfactory results, it is interesting to notice (Fig. 4.8) that all the cases show the introduction of annoying artifacts. As we can observe the Frost filter produces a light blur version of the speckle one, so it does not seem to reduce the speckle at all. The image filtered by SA-WBMMAE, the wavelet homomorphic shrinkage algorithm, presents strong artifacts characterizing the wavelet transform, which are smoothed by MAP-S, through the pre-classification of subband coefficients. Both PPB and SAR-BM3D reduce speckle and at the same time introduce artifacts, more marked for the latter. The two homomorphic versions H-PPB and H-BM3D show these artifacts amplified.

4.3.2 Edges image

The edges image is obtained, as we say in the previous section, by four adjacent homogeneous areas with different electromagnetic parameters: this causes different intensity returns. This is a very interesting case because, modeling the presence of discontinuities in SAR signals, can be used to compare the despeckling algorithms regarding to the preservation of edges. In this case the measure of SNR on the whole image is poor and provides no information about the structure. As consequence, we apply after the denoising step the standard Canny edge detector, optimizing its characteristic parameters on each filtered image, in order to have a comparison in the same conditions. The results of

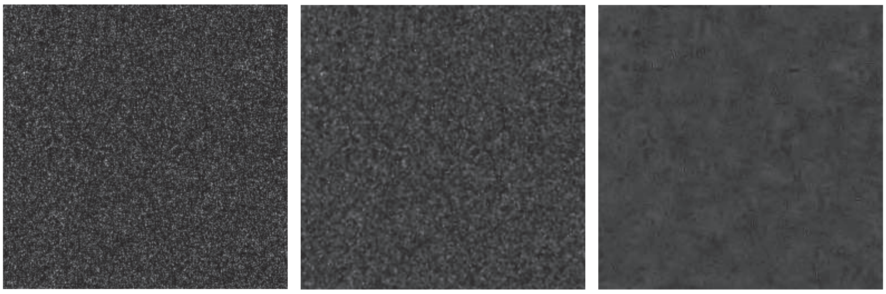

(a)Noisy image (b)Frost (c)SA-WBMMAE

(d)MAP-S (e)Original image (f)PPB

(g)H-PPB (h)SAR-BM3D (i)H-BM3D

Figure 4.8: Homogeneous filtered images.

the despeckling processing and of the edge detector are shown in Figs. 4.9 and 4.10.

As we can observe, the results in the four adjacent areas are the same respect the ones obtained for the homogeneous case. The relevant problem is the behavior of the techniques on the edge. Looking at the edge detector results we can see all the techniques perform quite well with not so relevant differences.

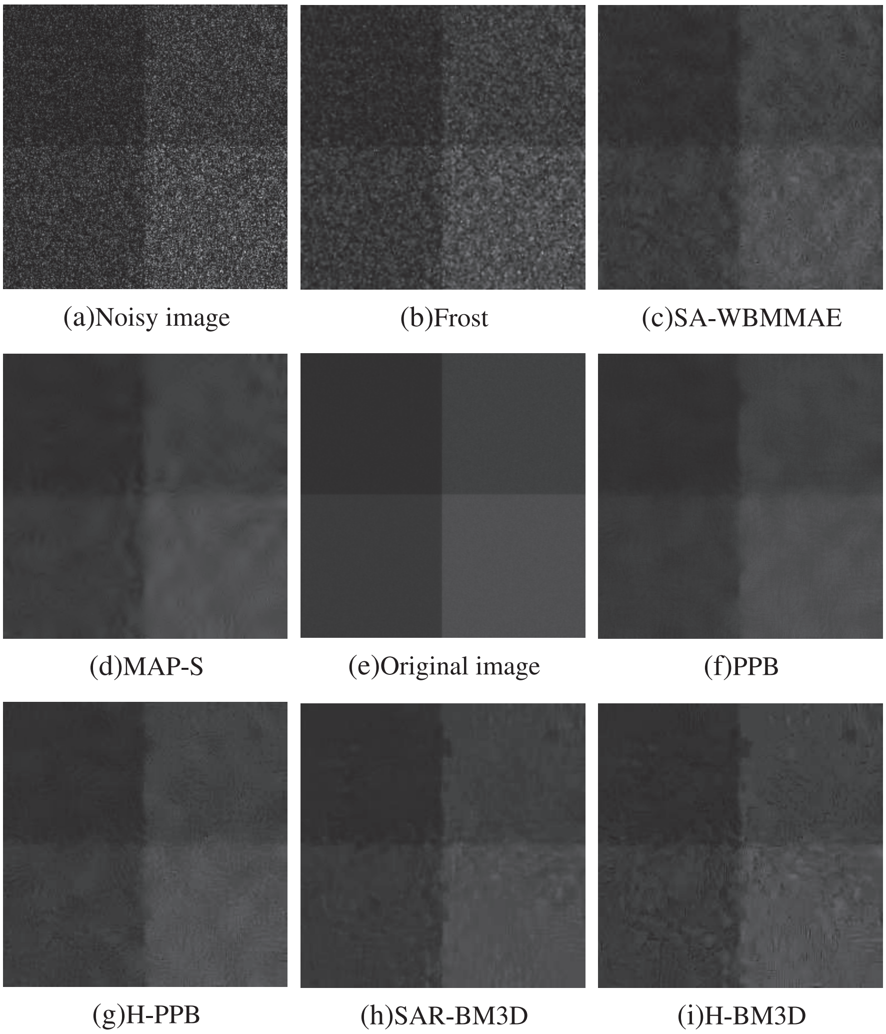
(a)Noisy image (b)Frost (c)SA-WBMMAE

(d)MAP-S (e)Original image (f)PPB

(g)H-PPB (h)SAR-BM3D (i)H-BM3D

Figure 4.9: Edges filtered images.

This means that some more than others the algorithms preserve the gray level contrast of the edges, depending on the artifacts and blurring effects introduced. A problem to consider is that the edges are obtained by discontinuities in the gray levels, thus they are not a real structure. Moreover because of the peculiarity of the SAR data, at the edges there are interferences between the impulsive response of the SAR system, which is modeled by a $sinc(\cdot)$ func-

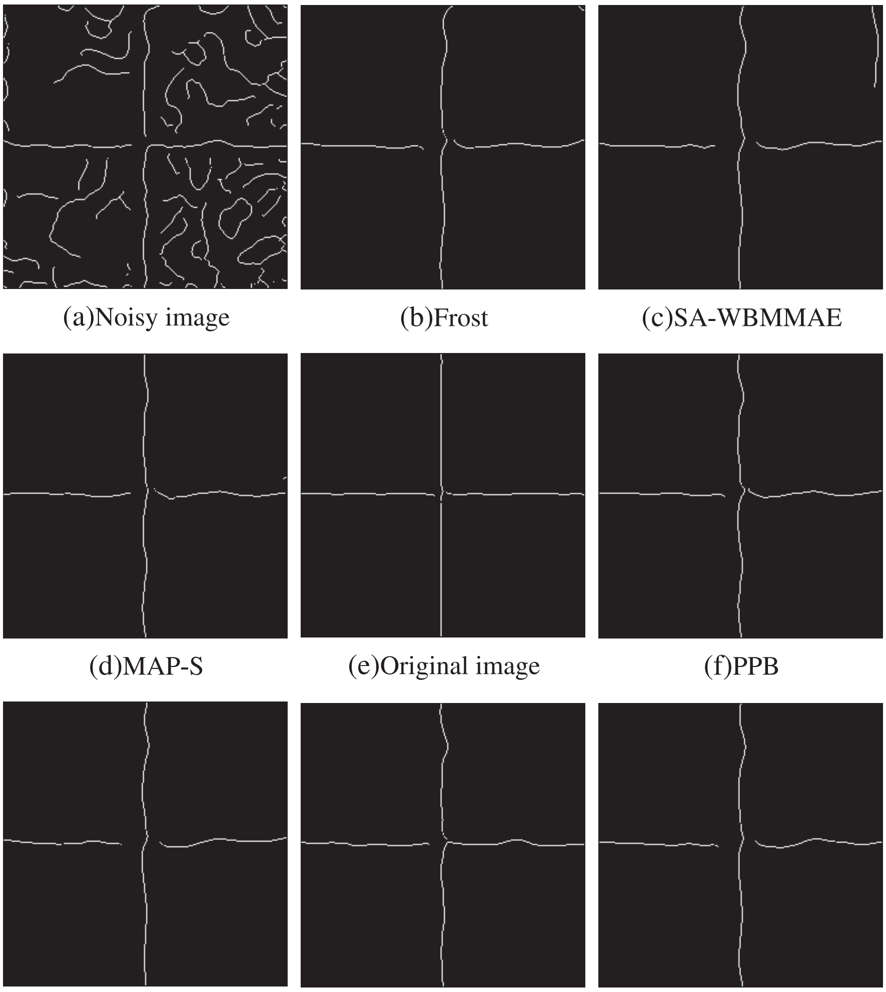
(a)Noisy image (b)Frost (c)SA-WBMMAE
(d)MAP-S (e)Original image (f)PPB
(g)H-PPB (h)SAR-BM3D (i)H-BM3D

Figure 4.10: Canny edge detector on filtered images.

tion and for what the secondary lobes are overlapped. As consequence, due the difficulties of the scenario, a useful parameter to consider together with the edge detector should be the SNR value, computed locally near the edge, or the mean value of the signal computed locally.

4.3.3 Dem image

The presence of textures in SAR images is very common so the analysis of this case is very useful. In fact, as we said above, structures such as woodlands, forests, waters or mountain profiles are always present in a SAR scenario. The main difference with the other previous cases is that all the points of the scene have the same electromagnetic characteristic, but different heights, providing more complex structure in the SAR images. So observing the dem images it is clear that a global SNR has not sense due the details spread over very different scales. In this case characterizing the autocorrelation function (acf) the texture itself, it is interesting and meaningful to observe the acf after the denoising step, to emphasize if a method introduces correlation. If this is the case the properties of the textures are not preserved. At this regard we have shown in Fig. 4.11 the range section acf of the speckled, clean reference and filtered images, for the more interesting techniques.

Observing the graphs we understand that the desired behavior should be to have a despeckled image acf as similar as possible to the reference one. All the techniques perform in this way, but with some differences. In fact, as we can see in Fig. 4.11, SAR-BM3D approximates in a better way the behavior of the clean reference acf, because it reduces the speckle without adding correlation on the original structure. Contrary, MAP-S produces an increase of the reference acf as we have shown in the graph (4.11): in fact, the dashed curve outgos the solid one. This justifies the artifacts introduction comparing the filtered and the reference image (Fig. 4.12).

As regards PPB, by the graph we observe, instead, a poor performance because the filtered acf is decreased respect to the original one. This is the opposite issue because this means that PPB does not reconstruct well the structure, loosing some details. This statement is confirmed by analyzing the ratio image R and its acf. Indeed the ratio image, as we said in the previous chapter is ideally the speckle, by the multiplicative model. So this image must be consistent with the speckle and so the presence of geometric structures are caused by a detail loss. At this regard we show the ratio image and its ideally and estimates acfs in Figs. 4.13 and 4.14.

As we can observe from the Fig. 4.13 PPB reduces the speckle but at the same time erases some features of the image structures. From the ratio image of MAP-S it is clear that also this technique in the dem images reduces the speckle but destroys some geometric structures characterizing the dem case. Instead SAR-BM3D (Fig. 4.14) and H-BM3D do not show this problem.

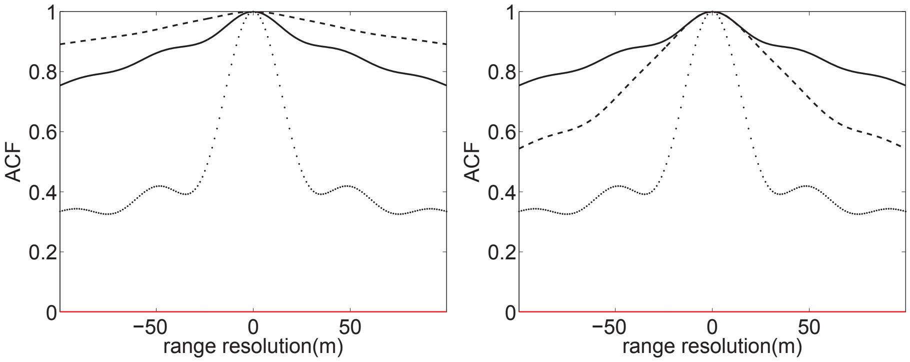

(a)MAP-S (b)PPB

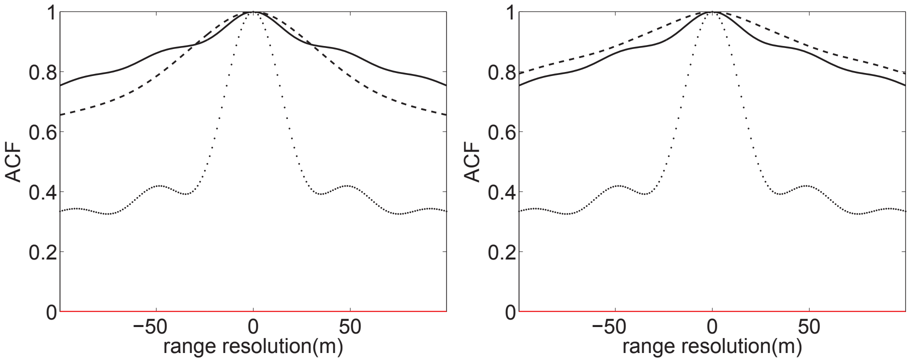

(c)SAR-BM3D (d)H-BM3D

Figure 4.11: Dem: original $(-)$, noisy $(\cdots)$ and filtered images $(--)$ acfs.

4.3.4 Corner reflector image

Corner reflectors or bright points are a very important features of the SAR images. In fact, these points are used, as a reference, to co-register SAR data, to correct some types of distortions and so on. So a good denoising technique has to reduce speckle but has to preserve corner reflectors too. Being the corner reflector a point in a complex SAR image, it appears as a sinc both in azimuth and in range coordinates. In fact, a SAR system maps points into $sinc(\cdot)$ with lobes variable with the system resolution. Usually to measure the preservation of a $sinc(\cdot)$ the standard parameter is the PSLR (Peak to Side lobe Ratio), defined as:

$$PSLR = 10 * log_{10}(I_{LP}/I_{LL}) \tag{4.5}$$

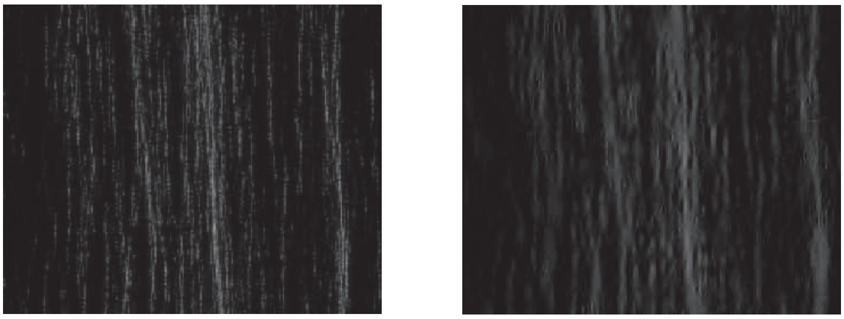

(a)Without speckle (b)MAP-S

Figure 4.12: Dem: MAP-S artifacts.

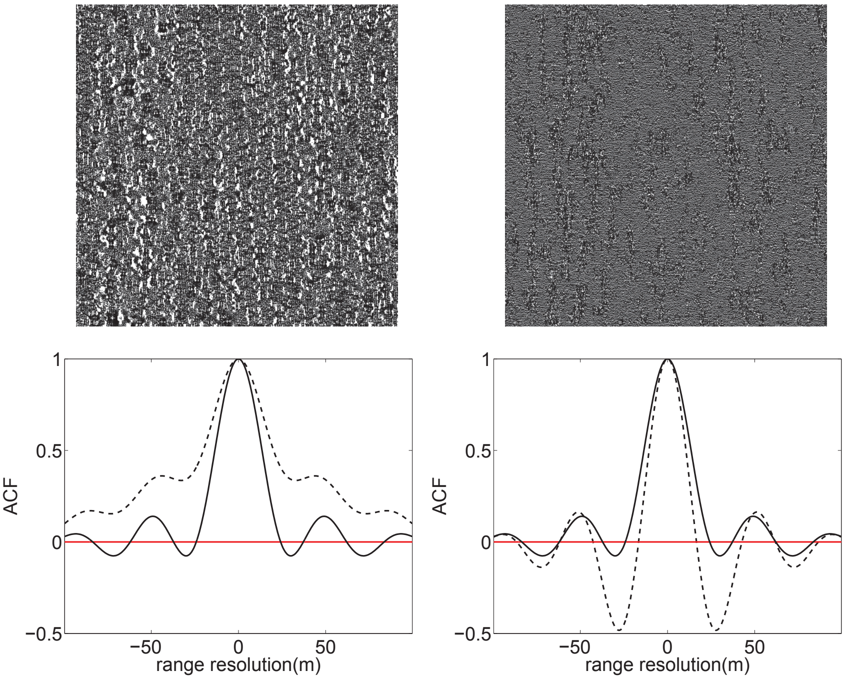

(a)MAP-S (b)PPB

Figure 4.13: Dem: ratio image and its acf.

where I_{LP} is the main lobe intensity and I_{LL} is the first side lobe intensity. A huge decrease of the PSLR indicates a reduction of the bright point and

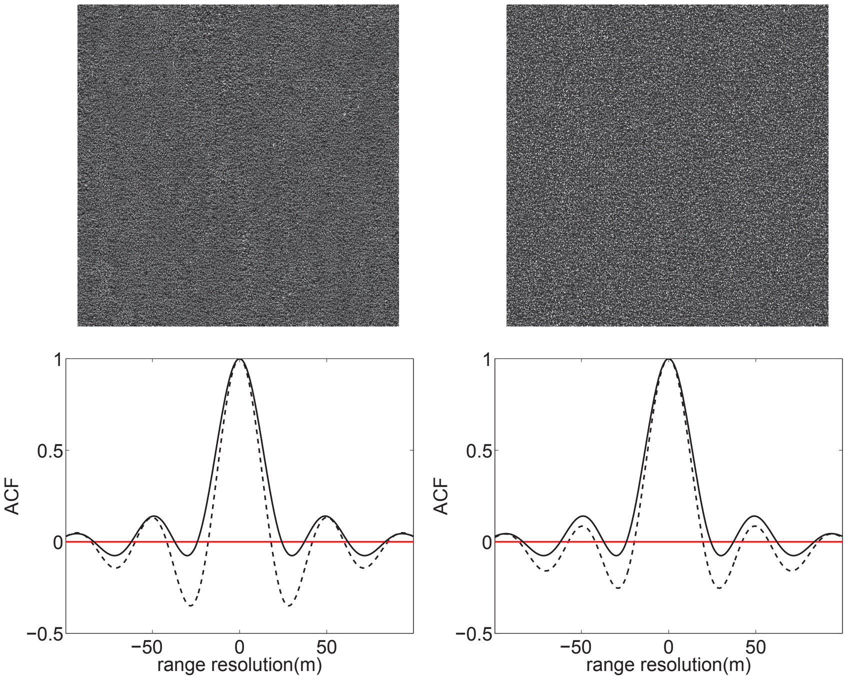

(c)SAR-BM3D

(d)H-BM3D

Figure 4.14: Dem: ratio image and its acf.

information of interest degradation. Here we do not consider the SAR complex data because of the despeckling techniques are able to tract only the absolute value of the data and not the phase. PSLR does not bear information at all. To overcome this problem we compute the contrast on the intensity image, defined as the ratio between the intensity of the corner reflector and all the pixels which surrounded it in a window of size $3x3$. If the contrast is preserved the point target is already considered as a corner reflector. We could also consider only the mean intensity value of the point target. Here we have shown the contrast in Tab. 4.2.

By the table, the better value of the contrast is provided by the Frost filter, because as we said previously the Frost filter does not reduce the speckle at all, so does not modify the corner reflector. MAP-S value is also good but in this case the value presents an increase justified by the rationale of the technique which through a pre-classification of the SAR data does not processes corner reflectors, while filters the surrounding areas. A good result is achieved by the

	Contrast
Noisy	23.99
Frost	21.64
SA-WBMMAE	3.12
MAP-S	26.70
PPB	9.51
SAR-BM3D	**17.00**
H-PPB	2.95
H-BM3D	12.25

Table 4.2: Contrast values computed on the corner intensity image

SAR-BM3D algorithm, which follows the previous two, while the others like PPB and the homomorphic approaches do not perform very well. To confirm these results we report the azimuth and range section of the filtered corner compared with the clean reference ones, for PPB, MAP-S and SAR-BM3D Fig. 4.15.

Notice by the graph that PPB produces a strange trend in azimuth sections where the side lobes on the left of the main one are deleted.

4.3.5 Building image

The last case is the image of a building on a typical urban background. In the last years the interest of analyzing urban area and high resolution SAR image is increased. A common application in this context is height retrieval of buildings from high resolution SAR image [70]. In [70] it is explained how to realize this task. A very important parameter to compute the height of the building is the mean value of the double reflection line (drl). The double reflection contribute is due to the building's corner in the SAR beam. Therefore in this case it is very important to check, after the denoising step, if the double reflection contribute is preserved. In order to select the best technique in this sense we have computed and shown in Tab. 4.3 the mean value along the white line in Fig. 4.7, which represents the double reflection line. As we can observe by the table, MAP-S is best techniques in this case. This is due to the fact that MAP-S, as we said above, exploits a classification of the wavelet coefficients before the processing in three main classes: homogeneous, heterogeneous and more heterogenous one. As consequence, the values classified as more heterogeneous have not processed at all. A very good value of the drl is due to SAR-BM3D, which although exploits denoising in the white area, preserving

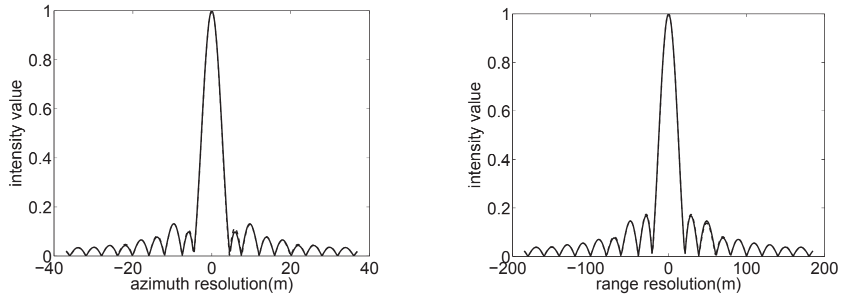

(a)MAP-S az (b)MAP-S r

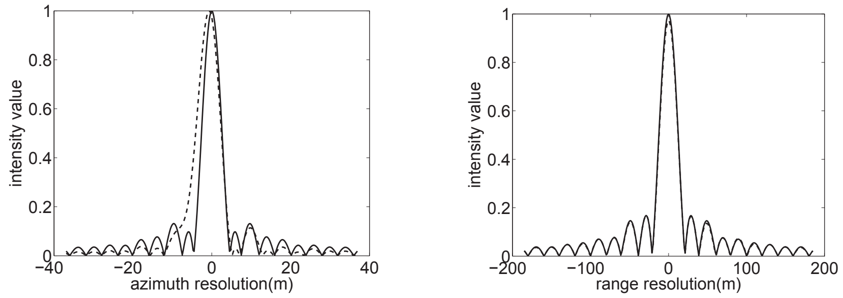

(c)PPB az (d)PPB r

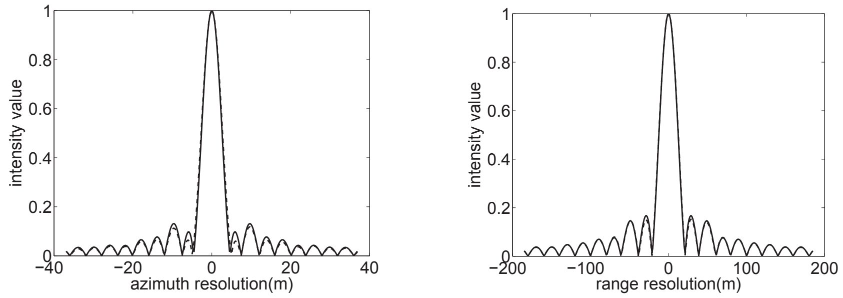

(e)SAR-BM3D az (f)SAR-BM3D r

Figure 4.15: Corner: original (−) and processed (−−) (az) and (r) sections.

at the same time very well the drl intensity value. We also emphasize that PPB gives a low value to indicate an anomaly, while the homomorphic approaches H-PPB and H-BM3D increase the value. Thus very interesting are the filtered image for MAP-S, SAR-BM3D and PPB and the azimuth (az) and range (r) Fig. 4.16.

By the figure it is clear the very strange behavior of PPB, which creates

	drl
Noisy	9.20e+5
Frost	6.26e+5
SA-WBMMAE	7.06e+5
MAP-S	**9.20e+5**
PPB	7.40e+5
SAR-BM3D	9.00e+5
H-PPB	1.09e+6
H-BM3D	1.02e+6

Table 4.3: Drl values

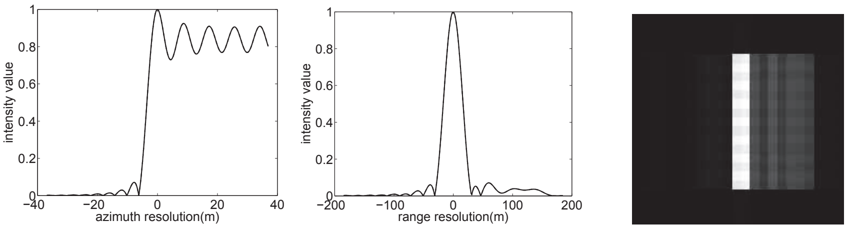

(a)MAP-S az (b)MAP-S r (c)MAP-S zoom

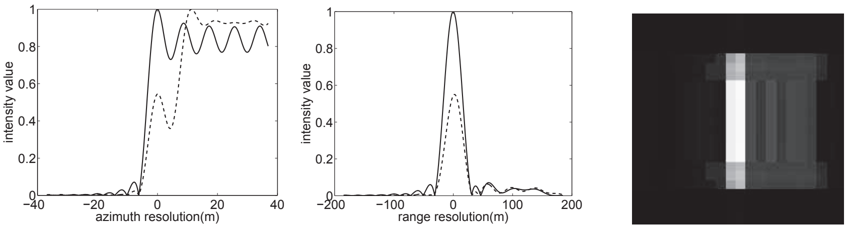

(d)PPB az (e)PPB r (f)PPB zoom

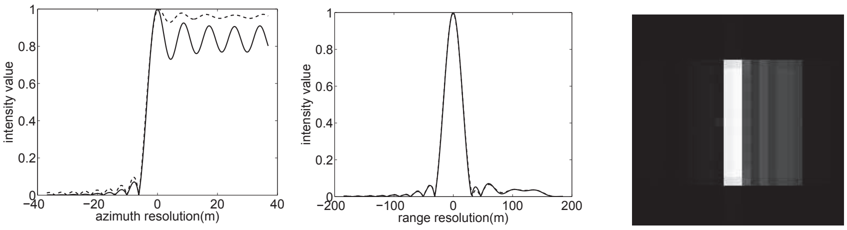

(g)SAR-BM3D az (h)SAR-BM3D r (i)SAR-BM3D zoom

Figure 4.16: Building: original (−) and processed (−−) (az) and (r) sections.

artifacts on the double reflection line.

Conclusions

Speckle in SAR images degrades the performance of image processing task in many fields of application. As a matter of facts, we need a suitable filtering to reduce the noise but at the same time we want to preserve all the relevant features of the scene. Furthermore there is no objective quality assessment of despeckling for the real SAR images. In this thesis we have proposed an innovative and very promising algorithm for SAR image despeckling and guidelines to obtain an objective comparison between the proposed and other despeckling algorithms.

The proposed algorithm SAR-BM3D, combines the concepts of non-local filtering and wavelet domain transform, adapting them to the statistical features of the SAR. The choice of the similarity measure to collect the patches has been done taking into account the probabilistic distribution of speckle. This choice, combined with the wavelet shrinkage in the 3D domain, which is derived from the additive signal-dependent model following a local linear MMSE estimation approach, are the major innovations introduced in SAR-BM3D. Results on images corrupted by simulated speckle are satisfactory, with a PSNR gain of 1-2 dB over the best reference algorithms to date. The analysis carried out on a synthetic image to evaluate the preservation of structures such as bars and target points show similar improvements. Experiments on actual SAR images are encouraging, as the proposed technique seems to have a better capacity to preserve relevant details reducing the speckle in homogeneous areas.

Several aspects of the proposed algorithm may still be improved. In particular, performance analysis showed different results when the algorithm is applied on simulated or real SAR images; the reason behind is that the speckle statistics of actual SAR images, especially at high resolution, often deviate from the simplified model used in this work, as well as in most of the literature. As future improvement the algorithm could be optimized for correlated speckle.

With reference to the performance assessment we have selected and simulated, with the cooperation of the remote sensing group, five canonical test cases, which comprise homogenous area, edges, corner reflector, natural mountain profile and a building common in urban areas. These cases are very useful to extract reliable information about the despeckling performance in more complex cases. We have exploited a detailed analysis, developing measures ad hoc for each case. Through this analysis we have highlighted that parameters such as Signal to Noise Ratio (SNR) or Minimum Square Error (MSE), usually used in many image processing tasks, are not always effective in despeckling procedures. In fact, for the homogeneous case the relevance of MSE or ENL is evident, in other cases such as edges or mountain profiles this parameter of measurement become useless. For edges we showed that more interesting parameters are a local SNR and the preservation of the edges, which is measured through an edge detector. Instead a SAR image of a digital elevation model, like a mountain, characterized by points at different heights, presents effects such as layover or foreshortening, and thus very complex structures. In this case the autocorrelation functions of the filtered and reference images give information about the correlation and then artifacts introduced by the despeckling techniques. Similar argumentations are developed in case of corner reflector and building, more common in the high resolution SAR images of urban area. So we have proposed guidelines to compare despeckling techniques giving the simulated cases and the ad hoc measures.

Further improvements in this context regard the possibility to introduce other criteria to compare the performance for each test case and the possibility to simulate more complex scenes to analyze after the despeckling processing.

Bibliography

[1] C. Oliver and S. Quegan, *Understanding Synthetic Aperture Radar Images*. SciTech, 2004.

[2] D. Riccio, "Lessons of remote sensing and electromagnetic diagnostic," 2005.

[3] J. Goodman, "Speckle with a finite number of steps," *Applied Optics*, vol. 47, no. 4, pp. A111–118, Feb. 2008.

[4] G. Poggi, A. R. P. Ragozini, and L. Verdoliva, "Compression of SAR data through range focusing and variable-rate vector quantization," *IEEE Transactions on Geoscience and Remote Sensing*, vol. 38, pp. 1282–1289, May 2000.

[5] C. D'Elia, G. Poggi, and L. Verdoliva, "Compression of SAR raw data through range focusing and variable-rate trellis-coded quantization," *IEEE Transactions on Image Processing*, vol. 10, pp. 1278–1287, Sep. 2001.

[6] S. Quegan, "Interpolation and sampling in sar images," *IEEE Transactions on Geoscience and Remote Sensing*, vol. 28, no. 4, pp. 641–646, 1990.

[7] H. H. Arsenault and G. April, "Properties of speckle integrated with a finite aperture and logarithmically transformed," *J. Opt. Soc. Am.*, vol. 66, no. 11, pp. 1160–1163, 1976.

[8] H. Xie, L. Pierce, and F. Ulaby, "Statistical properties of logarithmically transformed speckle," *IEEE Transactions on Geoscience and Remote Sensing*, vol. 40, no. 3, pp. 721–727, Mar. 2002.

[9] J. S. Lee, “Digital image enhancement and noise filtering by use of local statistics,” *IEEE Transactions on Pattern Analysis and Machine Intelligence*, vol. 2, pp. 165–168, 1980.

[10] ——, “Refined filtering of image noise using local statistics,” *Comput. Graph. Image Process.*, vol. 15, pp. 380–389, 1981.

[11] V. S. Frost, J. A. Stiles, K. S. Shanmugan, and J. C. Holtzman, “A model for radar images and its application to adaptive digital filtering of multiplicative noise,” *IEEE Transactions on Pattern Analysis and Machine Intelligence*, vol. PAMI-4, no. 2, pp. 157–166, Mar. 1982.

[12] D. T. Kuan, A. A. Sawchuk, T. C. Strand, and P. Chavel, “Adaptive noise smoothing filter for images with signal-dependent noise,” *IEEE Transactions on Pattern Analysis and Machine Intelligence*, vol. 7, pp. 165–177, Feb. 1985.

[13] R. Touzi, A. Lopes, and P. Bousquet, “A statistical and geometrical edge detector for sar images,” *IEEE Transactions on Geoscience and Remote Sensing*, vol. 26, no. 6, pp. 764–773, Nov. 1988.

[14] A. Lopes, R. Touzi, and E. Nezry, “Adaptive speckle filters and scene heterogeneity,” *IEEE Transactions on Geoscience and Remote Sensing*, vol. 28, pp. 992–1000, Nov. 1990.

[15] R. Touzi, “A review of speckle filtering in the context of estimation theory,” *IEEE Transactions on Geoscience and Remote Sensing*, vol. 40, no. 11, pp. 2392–2404, Nov. 2002.

[16] D. T. Kuan, A. A. Sawchuk, T. C. Strand, and P. Chavel, “Adaptive restoration of images with speckle,” *IEEE Transactions on Acoustics, Speech, and Signal Processing*, vol. 35, pp. 373–383, Jan. 1987.

[17] S. M. Kay, *Fundamentals of statistical signal processing: estimation theory*. Englewood Cliffs, NJ: Prentice Hall, 1993.

[18] A. Lopes, E. Nezry, R. Touzi, and H.Laur, “Maximum a posteriori speckle filtering and first order texture models in sar images,” in *Proceedings of IEEE International Geoscience and Remote Sensing Symposium*, vol. 3, May 1990, pp. 2409–2412.

[19] E. Nezry, A. Lopes, and R. Touzi, “Detection of structural and textural features for sar image filtering,” in *Proceedings of IEEE International Geoscience and Remote Sensing Symposium*, vol. 3, 1991, pp. 2169–2172.

[20] G. Gao, “Statistical modeling of sar images: a survey,” *Sensors*, pp. 775–794, Jan. 2010.

[21] I. Daubechies, “Orthonormal bases of compactly supported wavelets,” *Commun. Pure Appl. Math.*, vol. 41, pp. 909–996, 1988.

[22] S. Mallat, “A theory for multiresolution signal decomposition: the wavelet representation,” *IEEE Transactions on Pattern Analysis and Machine Intelligence*, vol. 11, no. 7, pp. 674–693, Jul. 1989.

[23] D. Donoho, “De-noising by soft-thresholding,” *IEEE Transactions on Information Theory*, vol. 41, no. 3, pp. 613–627, May 1995.

[24] H. Guo, J. Odegard, M. Lang, R. Gopinath, L. Selesnick, and C. Burrus, “Wavelet based speckle reduction with application to sar based atd/r,” in *Proceedings of IEEE Internantional Conference on Image Processing*, vol. 1, 1994, pp. 75–79.

[25] L. Gagnon and A. Jouan, “Speckle filtering of sar images-a comparative study between complex wavelet-based and standard filters,” in *Proc. SPIE*, vol. 3169, 1997, pp. 80–91.

[26] J. Sveinsson and J. Benediktsson, “Almost translation invariant wavelet transformations for speckle reduction of sar images,” *IEEE Transactions on Geoscience and Remote Sensing*, vol. 41, no. 10, pp. 2404–2408, Oct. 2003.

[27] S.Fukuda and H.Hirosawa, “Smoothing effect of wavelet-based speckle filtering: the haar basis case,” *IEEE Transactions on Geoscience and Remote Sensing*, vol. 37, pp. 1168–1172, Mar. 1999.

[28] A. Achim, P. Tsakalides, and A. Bezarianos, “Sar image denoising via bayesian wavelet shrinkage based on heavy-tailed modeling,” *IEEE Transactions on Geoscience and Remote Sensing*, vol. 41, no. 8, pp. 1773–1784, Aug. 2003.

[29] S. Solbø and T. Eltoft, “Homomorphic wavelet-based statistical despeckling of sar images,” *IEEE Transactions on Geoscience and Remote Sensing*, vol. 42, no. 4, pp. 711–721, Apr. 2004.

[30] M. Bhuiyan, M. Ahmad, and M. Swamy, “Spatially adaptive wavelet based method using the cauchy prior for denoising the sar images,” *IEEE Transactions on Circuits and Systems for Video Technology*, vol. 17, no. 4, pp. 500–507, Apr. 2007.

[31] H. Xie, L. Pierce, and F. Ulaby, “Sar speckle reduction using wavelet denoising and markov random field modeling,” *IEEE Transactions on Geoscience and Remote Sensing*, vol. 40, pp. 2196–2212, Oct. 2002.

[32] ——, “Despeckling sar images using a low complexity wavelet denoising process,” in *Proceedings of IEEE International Geoscience and Remote Sensing Symposium*, vol. 1, Nov. 2002, pp. 321–324.

[33] R. Öktem and K. Egizarian, “Transform domain algorithm for reducing effect of film-grain noise in image compression,” *Electronic Letters*, vol. 35, no. 21, pp. 1830–1831, Oct. 1999.

[34] F. Argenti and A. Alparone, “Speckle removal from sar images in the undecimated wavelet domain,” *IEEE Transactions on Geoscience and Remote Sensing*, vol. 40, pp. 2363–2374, Nov. 2002.

[35] M. Dai, C. Peng, A. K. Chan, and D. Loguinov, “Bayesian wavelet shrinkage with edge detection for sar image despeckling,” *IEEE Transactions on Geoscience and Remote Sensing*, vol. 42, no. 8, pp. 1642–1648, Aug. 2004.

[36] I. Daubechies, *Ten Lectures on Wavelets*. Society for Industrial and Applied Mathematics, 1992.

[37] R. Coifman and D. L. Donoho, “Translation-invariant de-noising,” ser. Lecture Notes in Statistics, A. Antoniadis, Ed. Berlin, Germany: Springer-Verlag, pp. 125–150, 1995.

[38] S.Foucher, G.B.Bénié, and J.M.Boucher, “Multiscale map filtering of sar images,” *IEEE Transactions on Image Processing*, vol. 10, pp. 49–60, Jan. 2001.

[39] F. Argenti, T. Bianchi, and A. Alparone, “Multiresolution map despeckling of sar images based on locally adaptive generalized gaussian pdf modeling,” *IEEE Transactions on Image Processing*, vol. 15, no. 11, pp. 3385–3399, Nov. 2006.

[40] S. Solbø and T. Eltoft, “Γ-WMAP: A statistical speckle filter operating in the wavelet domain,” *Int. J. Remote Sens.*, vol. 25, no. 5, pp. 1019–1036, Mar. 2004.

[41] B. Y. S. G. Chang and M. Vetterli, “Adaptive wavelet thresholding for image denoising and compression,” *IEEE Transactions on Image Processing*, vol. 9, no. 9, p. 15321546, Sep. 2000.

[42] F. Argenti, T. Bianchi, and A. Alparone, “Segmentation-based map despeckling of sar images in the undecimated wavelet domain,” *IEEE Transactions on Geoscience and Remote Sensing*, vol. 46, no. 9, pp. 2728–2742, Sep. 2008.

[43] A. Buades, B. Coll, and J.M.Morel, “A review of image denoising algorithms, with a new one,” *Multiscale Model. Simul.*, vol. 4, no. 2, pp. 490–530, Jul. 2005.

[44] A. Efros and T. Leung, “Texture synthesis by non parametric sampling,” in *Proc. Int. Conf. Computer Vision*, vol. 2, 1999, pp. 1033–1038.

[45] V. Katkovnik, A. Foi, K. Egiazarian, and J. Astola, “From local kernel to nonlocal multiple-model image denoising,” *International Journal of Computer Vision*, vol. 86, no. 1, pp. 1–30, Jan. 2010.

[46] P. Coupé, P. Hellier, C. Kervrann, and C. Barillot, “Bayesian non local means-based speckle filtering,” in *5th IEEE International Symposium on Biomedical Imaging*, May 2008, pp. 1291–1294.

[47] H. Zhong, J. Xu, and L. Jiao, “Classification based nonlocal means despeckling for sar image,” in *proc. of SPIE*, vol. 7495, Oct. 2009.

[48] C. Deledalle, L. Denis, and F. Tupin, “Iterative weighted maximum likelihood denoising with probabilistic patch-based weights,” *IEEE Transactions on Image Processing*, vol. 18, no. 12, pp. 2661–2672, Dec. 2009.

[49] J. Polzehl and V. Spokoiny, “Propagation-separation approach for local likelihood estimation,” *Probability Theory and Related Fields*, vol. 135, no. 3, pp. 335–362, 2006.

[50] K. Dabov, A. Foi, V. Katkovnik, and K. Egiazarian, “Image denoising by sparse 3D transform-domain collaborative filtering,” *IEEE Transactions on Image Processing*, vol. 16, no. 8, pp. 2080–2095, Aug. 2007.

[51] S. Ghael, A. Sayeed, and R. Baraniuk, “Improved wavelet denoising via empirical wiener filtering,” in *Proc. SPIE*, vol. 5, Jul. 1997, pp. 389–399.

[52] S. Parrilli, M. Poderico, C. V. Angelino, and L. Verdoliva, “A nonlocal SAR image denoising algorithm based on LLMMSE wavelet shrinkage,” *IEEE Transactions on Geoscience and Remote Sensing*, vol. PP, pp. 1–11, 2011.

[53] S. Mallat, *A Wavelet Tour of Signal Processing*. Boston, MA: Academic, 1998.

[54] L. P. Yaroslavsky, *Digital picture processing, an introduction*. Berlin: Springer-Verlag, 1985.

[55] M. Poderico, S. Parrilli, G. Poggi, and L. Verdoliva, “Sigmoid shrinkage for BM3D denoising algorithm,” in *Proceedings of IEEE Workshop on Multimedia Signal Processing*, Oct. 2010.

[56] M. Matrecano, M. Poderico, G. Poggi, M. Romano, and M. Cesarelli, “Application of denoising techniques to micro-tomographic images,” in *Proceedings of IEEE International Conference on Information Technology and Applications in Biomedicine*, Nov. 2010.

[57] H. Mäkitalo, A. Foi, D. Fevralev, and V. Lukin, “Denoising of single-look sar images based on variance stabilization and nonlocal filters,” in *Proc. Int. Conf. Math. Meth. Electromagn. Th., MMET*, Sep. 2010.

[58] M. Lang, H. Guo, and J. E. Odegard, “Noise reduction using undecimated discrete wavelet transform,” *IEEE Signal Processing Letters*, vol. 3, no. 1, pp. 10–12, Jan. 1996.

[59] M. Elad, “Why simple shrinkage is still relevant for redundant representations?” *IEEE Transactions on Information Theory*, vol. 52, no. 12, pp. 5559–5569, Nov. 2006.

[60] L. Zhang, P. Bao, and X. Wu, “Multiscale lmmse-based image denoising with optimal wavelet selection,” *IEEE Transactions on Circuits and Systems for Video Technology*, vol. 15, no. 4, pp. 469–481, Apr. 2005.

[61] Y. Matsushita and S. Lin, “A probabilistic intensity similarity measure based on noise distributions,” in *IEEE Conference on Computer Vision and Pattern Recognition*, 2007, pp. 1–8.

[62] M. K. Mihcak, I. Kozintsev, and K. Ramchandran, “Spatially adaptive statistical modeling of wavelet image coefficients and its application to denoising,” in *Proceedings of IEEE International Conference on Acoustics, Speech and Signal Processing*, Phoenix, AZ, USA, Mar. 1999, pp. 3253–3256.

[63] F. Jin, P. Fieguth, L. Winger, and E. Jernigan, “Adaptive wiener filtering of noisy images and image sequences,” in *Proceedings of IEEE Internantional Conference on Image Processing*, vol. 3, Sep. 2003, pp. 349–352.

[64] M. Kazubek, “Wavelet domain image denoising by thresholding and wiener filtering,” *IEEE Signal Processing Letters*, vol. 10, pp. 324–326, Nov. 2003.

[65] J. S. Lee, L. Jurkevich, P. Dewaele, and P. W. ans A.Oosterlinck, “Speckle filtering of synthetic aperture radar images: A review,” *Remote Sensing Reviews*, vol. 8, no. 4, pp. 313–340, jan 1994.

[66] G. Franceschetti, M. Migliaccio, D. Riccio, and G. Schirinzi, “SARAS: a SAR raw signal simulator,” *IEEE Transactions on Geoscience and Remote Sensing*, vol. 30, no. 1, pp. 110–123, Jan. 1992.

[67] G. Franceschetti and D. Riccio, *Scattering, Natural Surfaces and Fractals*. Burlington, MA: Academic, 2007.

[68] R. K. Raney and G. J. Wessels, “Spatial considerations in SAR speckle consideration,” *Commun. Pure Appl. Math.*, vol. 26, no. 5, pp. 666–672, Sep. 1988.

[69] G. Franceschetti, A. Iodice, and D. Riccio, “A canonical problem in electromagnetic backscattering from buildings,” *IEEE Transactions on Geoscience and Remote Sensing*, vol. 40, no. 8, pp. 1787–1801, Aug. 2002.

[70] R. Guida, A. Iodice, and D. Riccio, “Height retrieval of isolated buildings from single high-resolution sar images,” *IEEE Transactions on Geoscience and Remote Sensing*, vol. 48, no. 7, pp. 2967–2979, Jul. 2010.